A Formal Bayesian Approach to SENSE Image Reconstruction

Chase J. Sakitis [a], Daniel B. Rowe [a], D. Andrew Brown [b]

[a] *Department of Mathematical and Statistical Sciences, Marquette University, Milwaukee Wisconsin, USA*
[b] *School of Mathematical and Statistical Sciences, Clemson University, Clemson, SC 29634, USA*

Abstract

In fMRI, capturing cognitive temporal dynamics is dependent on how quickly volume brain images are acquired. The sampling time for an array of spatial frequencies to reconstruct an image is the limiting factor in the fMRI process. Multi-coil SENSE image reconstruction is a parallel imaging technique that has greatly reduced image scan time. In SENSE image reconstruction, coil sensitivities are estimated once from *a priori* calibration images and used as fixed "known" coil sensitivities for image reconstruction of every subsequent image. This technique utilizes least squares estimation via the normal equation to evaluate voxel values in the reconstructed image. This method can cause difficulty in estimating voxel values if our design matrix is not positive definite. Here, we propose a Bayesian approach where prior distributions for the unaliased images, coil sensitivities, and uncertainty are assessed from the *a priori* calibration image information. Images and coil sensitivities are marginally estimated *a posteriori* via Iterated Conditional Modes algorithm and Markov chain Monte Carlo using Gibbs sampling. In addition, variability estimates and hypothesis testing is possible. This Bayesian SENSE (BSENSE) model utilizes prior image information to reconstruct images from the posterior distribution and is applied to simulated and experimental fMRI data. This BSENSE model sufficiently reconstructed a single slice image and a series of images without any artifacts from the simulated data and was replicated with magnitude-only task activation.

1. Introduction

1.1 Background

Magnetic Resonance Imaging (MRI) is a type of medical imaging device that creates internal anatomic body images using strong magnetic fields. Functional Magnetic Resonance Imaging (fMRI) was developed in the early 1990's as a technique to noninvasively observe the human brain in action (Bandettini et al, 1993). This procedure analyzes brain activity by detecting changes in the blood oxygenation using the blood-oxygen-level dependent (BOLD) contrast (Ogawa et al., 1990). When a neuron fires, the blood oxygenation changes in the proximity of the neuron and is thus a correlate for neuronal firing. In MRI, the machine does not directly measure voxel values and images. Measurements from the machine are arrays of complex-valued spatial frequencies called *k*-space (Kumar et al., 1975). Measuring full arrays of data for all the slices that shape the volume image typically takes about one to two seconds. These *k*-space values are then reconstructed into images using an inverse Fourier transform (IFT). The acquisition of *k*-spaces can take a considerable amount of time in the MRI process. A great deal of work has been dedicated to reducing the scan time of the MRI process by accelerating the number of images acquired per unit of time from its initial postulation. Hype et al., Pruessmann et al., and Griswold et al. all explore parallel techniques to reduce the scan time in MRI.

1.2 Previous Approaches

Historically, a single channel coil receiver has been utilized in fMRI to measure full-sampled *k*-space data arrays. Along with parallel utilization of multiple receiver coils, parallel imaging techniques began subsampling lines in-plane by skipping lines of *k*-space for an image, causing the reconstructed coil images to be aliased. GeneRalized Autocalibrating Partial Parallel Acquisition (GRAPPA) is a parallel imaging technique, introduced by Griswold et al., that operates on the subsampled *k*-space prior to the IFT. In 1999, Pruessmann et al. introduced SENSitivity Encoding (SENSE), another parallel imaging technique, which operates on the aliased images after the IFT. Both are major parallel imaging techniques developed to

unalias in-plane aliased images. The purpose of this research is to introduce a formal Bayesian approach to SENSE image reconstruction. The SENSE method uses simple linear regression with a fixed design matrix and unobserved parameters, which would be the unaliased voxel values, to model the data from the aliased reconstructed images. The unaliased voxels are estimated using the normal equations for the least squares solution. This approach for parameter estimation can be difficult because the design matrix, generally, is ill-conditioned which means it is not always positive definite. This becomes the motivation for a Bayesian approach, which will allow for a more general method for parameter estimation.

1.3 Overview

The second section of this paper will discuss the methods of this research. It will start with a general background in SENSE building up from a single-coil full-sampled *k*-space to a multi-coil sub-sampled *k*-space and discuss the complex-valued nature of the problem. This will lead into our approach and the mathematics behind the two Bayesian models. Section 3 will derive the assessment of the hyperparameters in our models, illustrate the simulated fMRI data for a single slice non-task image, and show the results for both models. Section 4 will look at the simulated results from a series of non-task images. In section 5, we will introduce task activation and cover simulated single slice results for both models. We will finish up in section 6 with an overview of the paper and a discussion of future work.

2. Methods

2.1 SENSE

To motivate our proposed approach, in this section we first consider single-coil full *k*-space inverse Fourier transform image reconstruction. Then the multi-coil full-sampled *k*-space IFT image reconstruction with SENSE image combination, and finally multi-coil sub-sampled *k*-space with SENSE image combination.

2.1.1 Single-Coil Full-Sampled *k*-Space Image Reconstruction

A single coil channel is shown in Figure 2.1 (left) with the *k*-space data being measured in a zig-zag fashion from left to right and bottom to top with turn around points at the end of each row (right side of Figure 2.1) omitted, thus creating a two-dimensional grid of spatial frequencies. Each

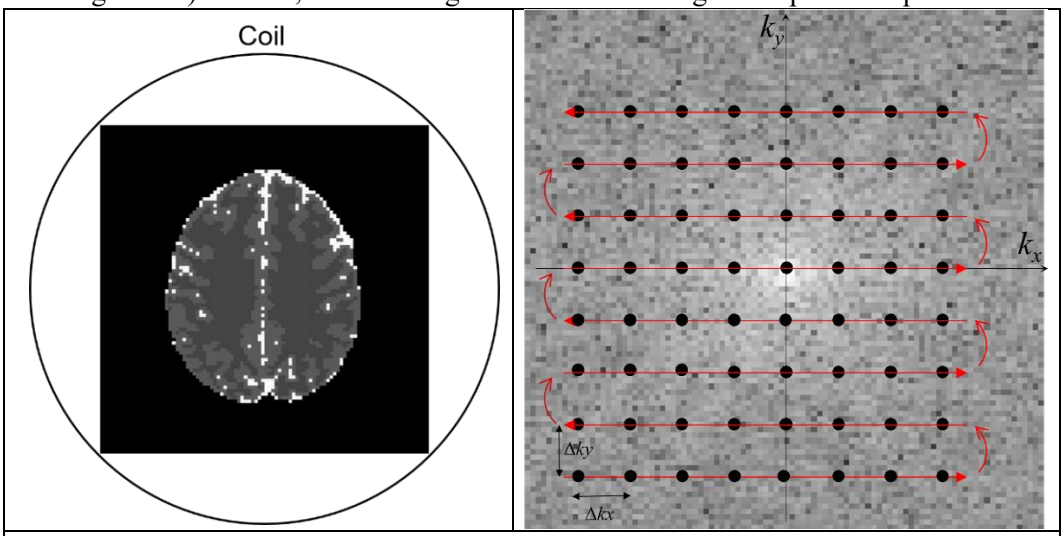

Figure 2.1: Single channel coil (left) and *k*-space zig-zag coverage (right).

point in the *k*-space contains spatial frequency and phase information about every pixel in the final reconstructed image meaning that the *k*-space is not one-to-one with the final image.

Since the *k*-space is complex-valued, as depicted in Figure 2.2 (column 2), there is a real part (first row) and an imaginary part (second row). An inverse Fourier transform matrix is depicted in Figure 2.2 (column 1) to illustrate the pre-multiplication of the *k*-space with a real part (first row) and an imaginary part (second row). The real part of the IFT matrix is a graphical depiction of the cosine waves at different frequencies,

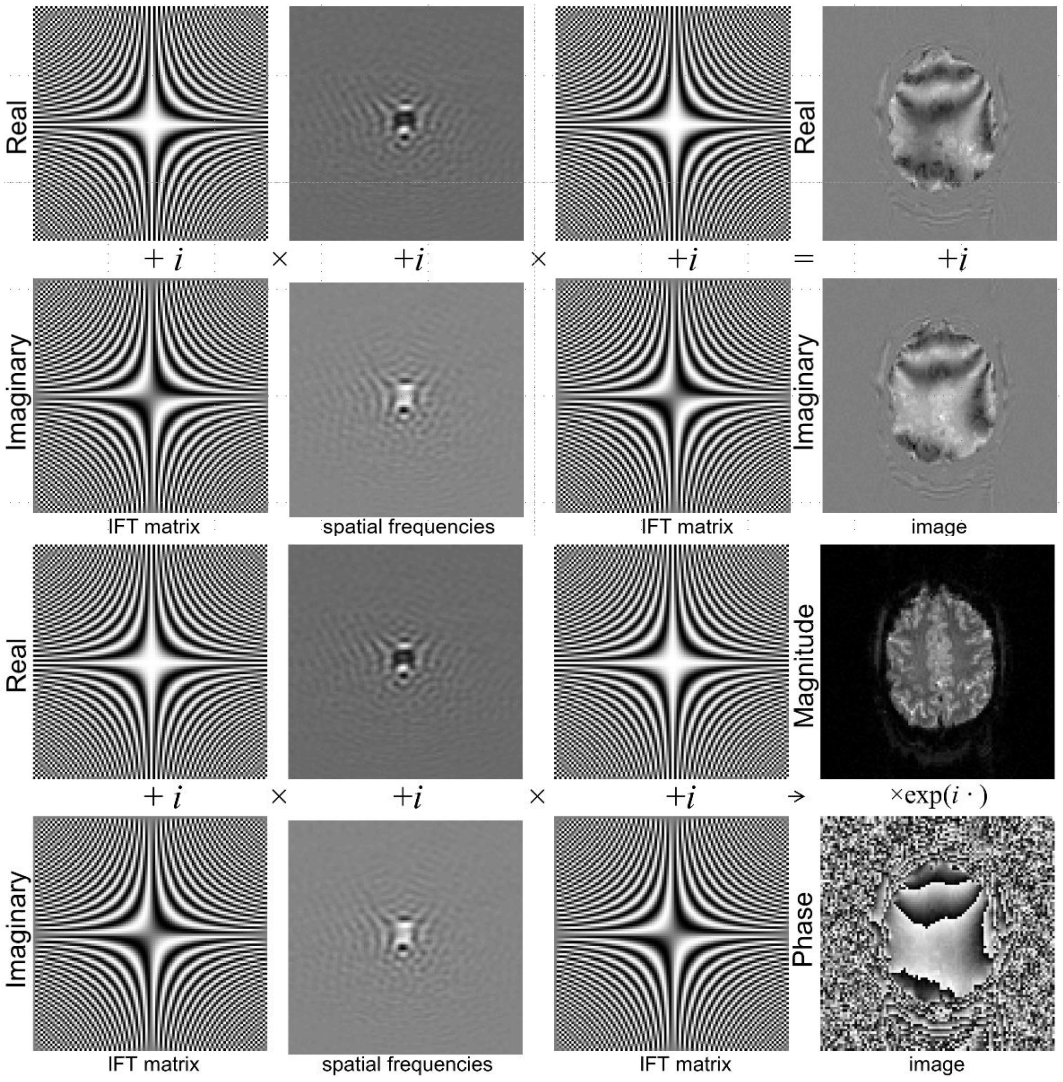

Figure 2.2: Inverse Fourier transform image reconstruction of a complex-valued *k*-space array to a complex-valued image (first and second row). Inverse Fourier transform image reconstruction of a complex-valued *k*-space array to a magnitude and phase image (third and fourth row).

and the imaginary part of the IFT matrix is a graphical depiction of the sine waves at different frequencies. Then the transpose of an IFT, depicted in Figure 2.2 (column 3), is used to post-multiply the *k*-space with a real part (first row) and an imaginary part (second row). The third (real parts) and fourth (imaginary parts) rows in Figure 2.2 display the same process expressed above with IFT in column 1, the *k*-space in column 2, and the transpose of the IFT in column 3. This results in a reconstructed image (column 4) with a real part (first row) and an imaginary part (second row). Since the magnitude (row 3, column 4) and the phase (row 4, column 4) of the reconstructed images are generally observed for fMRI analysis, they are also shown in Figure 2.2. This is simply a conversion to polar coordinates from Cartesian coordinates in the complex plane. Since our voxel values are complex, it forms a vector on a Cartesian grid with the real part indicating the length in the x-direction and the imaginary part indicating the length in the y-direction. Converting to polar coordinates would give us the magnitude (the length) and the phase (the angle) of the voxel vector. For this research, the concentration will be on Cartesian *k*-space sampling, with the conversion to polar coordinates used for depiction purposes. A series of these reconstructed images is produced while

the subject is performing a task and either the magnitude alone can be utilized for activation (Bandettini et al, 1993) or both the magnitude and phase (Rowe and Logan, 2004, and Rowe, 2005). In magnitude-only activation, we discard phase information which means we only analyze the change in length of the voxel vector. For magnitude and phase activation, we analyze the change in length and angle of the voxel vector. For this paper, we will focus on magnitude-only task activation.

2.1.2 Multi-Coil Full-Sampled *k*-Space Image Reconstruction

Instead of one coil receiver being used to acquire data to produce image slices, multiple coil arrays can be employed. An example of this is illustrated in Figure 2.3 (left) with $n_C = 4$ coil receivers. Increasing the number of sensitivity coils can provide better quality images and accelerates the acquisition of the images. Each of the four coils can measure a full-sampled *k*-space array as shown in Figure 2.3 (right) similar to how the *k*-space is sampled for a single coil.

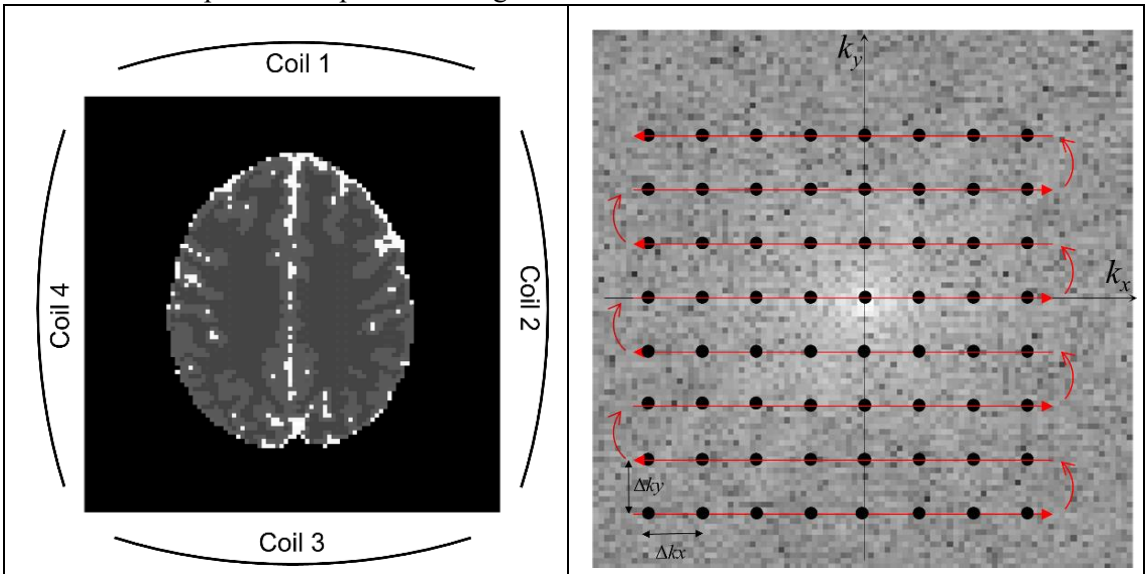

Figure 2.3: Four channel coil (left) and *k*-space zig-zag coverage (right).

Each local receiver coil possesses a depth sensitivity profile that is related to its size measuring a different sensitivity weighted version of the true slice. This means that each coil can only "see" parts of the object with a particular depth that gets weaker as we move farther from the coil. This is referred to the depth sensitivity profile which depends on the size of the coil and its location. In Figure 2.4 (middle center) is a true slice image with a particular voxel *v* indicated with a red circle. The depth sensitivity profile for coil 1 is given in Figure 2.4 (top) with unobserved voxel value *v* from the true slice and its unobserved coil sensitivity S_1 which is the weight that determines how strongly *v* shows in coil 1. Both S_1 and *v* are scalars. Coil 1 measures a *k*-space array that, after inverse Fourier transformation, is the true image point-wise multiplied by the sensitivity profile for coil 1, $a_1 = S_1 v$ as in Figure 2.4 (top right) where a_1 is the scalar weighted voxel value (observed coil measurement). This is the same process for the other three coils with coil 2, $a_2 = S_2 v$, in the bottom right of Figure 2.4, coil 3, $a_3 = S_3 v$, in the bottom left of Figure 2.4, and coil 4, $a_4 = S_4 v$, in the top left of Figure 2.4.

The $n_C = 4$ coil measurements create a system of equations which can be expressed as Eq. 2.1 where $a = [a_1, a_2, a_3, a_4]'$ is a $n_C \times 1$ vector of the observed coil measurements, $S = [S_1, S_2, S_3, S_4]'$ is a $n_C \times 1$ vector of the unobserved coil sensitivities, and v is the scalar unobserved true slice voxel value.

$$\begin{bmatrix} a_1 \\ a_2 \\ a_3 \\ a_4 \end{bmatrix} = \begin{bmatrix} S_1 \\ S_2 \\ S_3 \\ S_4 \end{bmatrix} v \qquad [2.1]$$

If we are able to obtain coil sensitivities estimate S, we can use the normal equation to obtain a least squares estimate of the true slice voxel v from Eq. 2.2. This process is repeated for each voxel in the image.

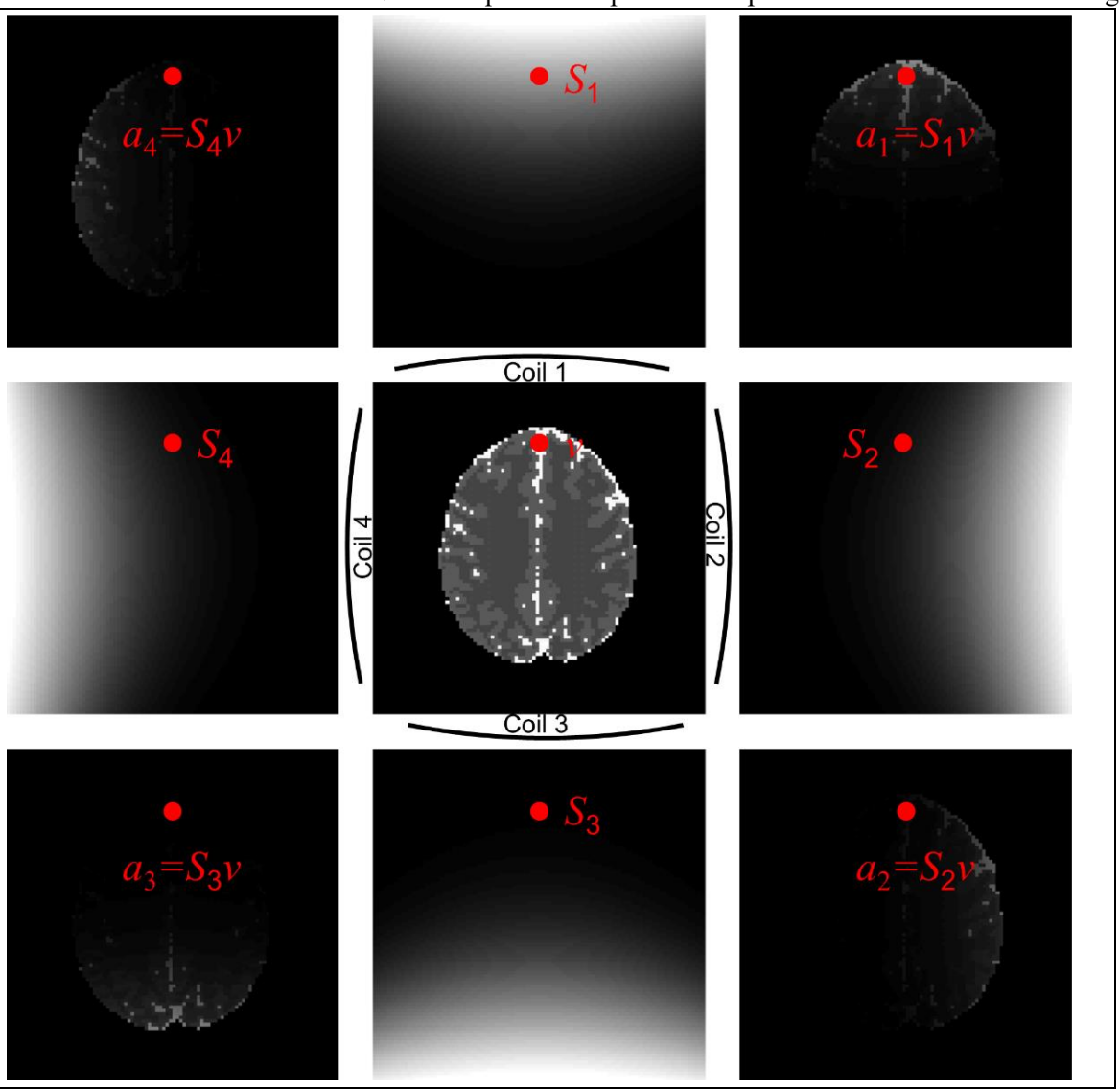

Figure 2.4: True slice image along with coil sensitivity profiles and sensitivity weighted true images.

$$\hat{v} = (S'S)^{-1}S'a \qquad [2.2]$$

2.1.3 Multi-Coil Sub-Sampled *k*-Space Image Reconstruction

As mentioned before, the goal is to accelerate the number of images acquired per unit of time. An intuitive solution to obtaining this goal is to travel faster through the *k*-space. However, according to Pruessmann et

al., physiological, and technical limitations of doing such have already been reached. Another idea is to measure less data and without losing the ability to form a full image. This can be accomplished by skipping lines in the *k*-space and not measuring the corresponding data values which under-samples, or sub-samples, the *k*-space. Skipping lines in the *k*-space introduces what is called an acceleration factor, or reduction factor. The acceleration factor indicates which lines of data in the *k*-space are measured and how many lines are skipped in *k*-space data acquisition. As shown in Figure 2.5 (right), with an acceleration factor of $n_A = 3$, every third line horizontally in the *k*-space is measured by skipping every two lines in the *k*-space. This acceleration factor will cause the reconstructed coil images to appear as if the full image was cut into three equal horizontal strips that are summed together. This happens because the Fourier transform cannot uniquely map the insufficiently sampled signals.

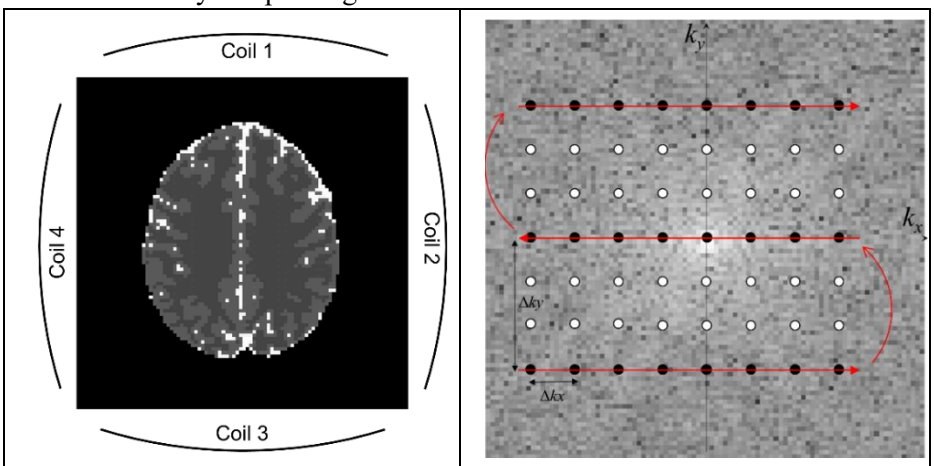

Figure 2.5: Four channel coil (left) and *k*-space zig-zag coverage (right).

Each local receiver coil, again, possesses a depth sensitivity profile that is related to its size measuring a different sensitivity weighted version of the true slice. In Figure 2.6 (middle center) is a true slice image with $n_A = 3$ voxels v_1, v_2, v_3 in corresponding locations relative to each strip.

Coil 1 measures a rectangular *k*-space array that after inverse Fourier transform reconstruction produces an aliased rectangular image that is the sum of three horizontal strips of the full true image as in Figure 2.6 (top right). In Figure 2.6 (top right) the true aliased image is the point-wise multiplication of the given voxel by the sensitivity profile for coil 1 summed for the three strips, $a_1 = S_{11}v_1 + S_{12}v_2 + S_{13}v_3$ where S_{11}, S_{12}, and S_{13} are the scalar weights that determines how strongly v_1, v_2, v_3, respectively, show in coil 1 and a_1 is the scalar weighted voxel value (observed coil measurement). Shown in Figure 2.6, this is the same process for the other three coils with coil 2 (bottom right) $a_2 = S_{21}v_1 + S_{22}v_2 + S_{23}v_3$, coil 3 (bottom left) $a_3 = S_{31}v_1 + S_{32}v_2 + S_{33}v_3$, and coil 4 (top left) $a_4 = S_{41}v_1 + S_{42}v_2 + S_{43}v_3$. Similar to Eq. 2.1, the $n_C = 4$ coil measurements create a system of equations which can be expressed as Eq. 2.3.

$$\begin{bmatrix} a_1 \\ a_2 \\ a_3 \\ a_4 \end{bmatrix} = \begin{bmatrix} S_{11} & S_{12} & S_{13} \\ S_{21} & S_{22} & S_{23} \\ S_{31} & S_{32} & S_{33} \\ S_{41} & S_{42} & S_{43} \end{bmatrix} \begin{bmatrix} v_1 \\ v_2 \\ v_3 \end{bmatrix} \qquad [2.3]$$

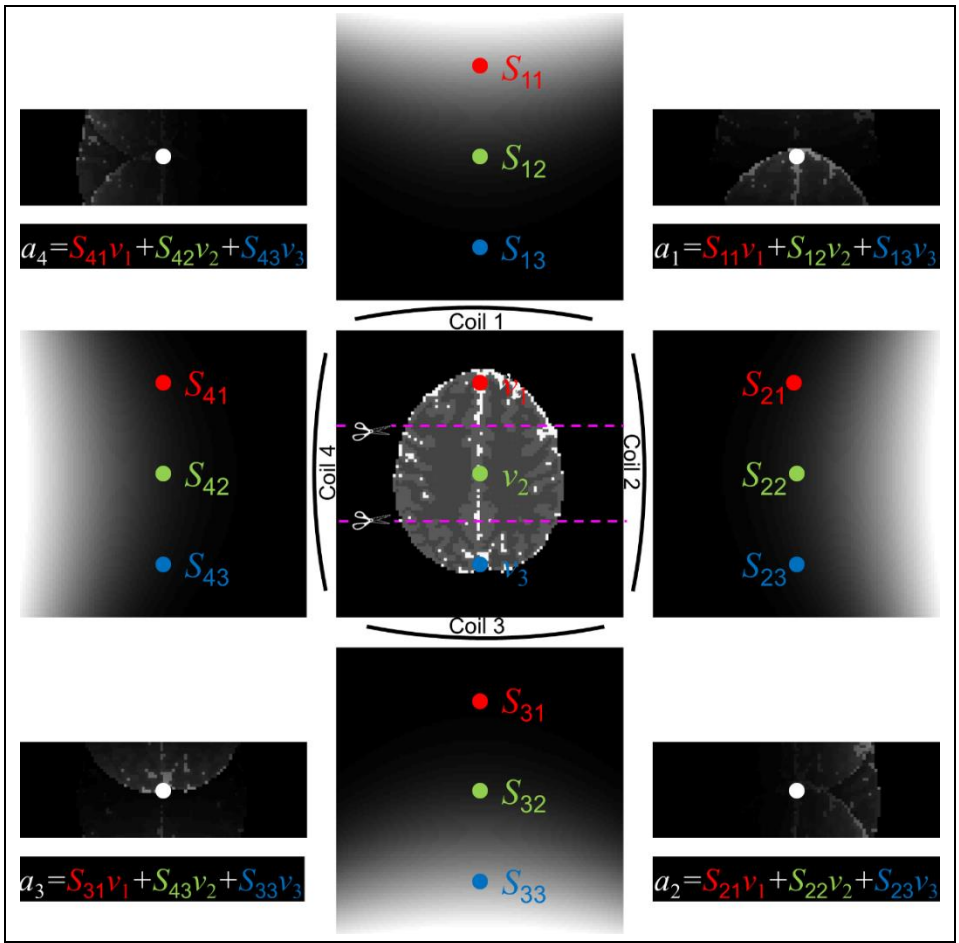

Figure 2.6: True slice image along with coil sensitivity profiles and sensitivity weighted true aliased images.

Where $a=[a_1,a_2,a_3,a_4]'$ is a $n_C \times 1$ vector of the observed coil measurements, $S=[[S_{11},S_{21},S_{31},S_{41}]',[S_{12},S_{22},S_{32},S_{42}]',[S_{13},S_{23},S_{33},S_{43}]']$ is a $n_C \times n_A$ matrix of the unobserved coil sensitivities, and $v=[v_1,v_2,v_3]'$ is a $n_A \times 1$ vector of the unobserved true slice voxel values. If we are able to obtain an estimate of the coil sensitivities S, we can obtain a least squares estimate of the n_A true slice voxel values v from Eq. 2.2. This process is repeated for each voxel in the aliased image.

2.1.4 Complex-Valued SENSE Image Reconstruction

We now consider a complex-valued version of the scenarios described in the previous subsections, as our goal is to analyze both the magnitude and phase information produced by the MRI scanner. Continuing the use of $n_C=4$ receiver coils shown in Figures 2.3 and 2.5 (left), the depth sensitivity profiles for each coil is complex-valued and not real-valued. So, each coil measures complex-valued weighted sensitivities of the true image slice depending on the location and size of the coil. Figure 2.7 shows the complex-valued image slices with $n_C=4$ coils (top, bottom, left, right) and their respective depth sensitivity to the true image slice (the four corners of the figure) like the illustration of Figure 2.4. A true image slice is displayed in Figure 2.7 (middle center) with a particular voxel $v=v_R+iv_I$, where i is the pure imaginary unit, indicated by red circles. The depth sensitivity profile for coil 1 is given in Figure 2.7 (top) with sensitivity $S_1=S_{1R}+iS_{1I}$ for voxel $v=v_R+iv_I$. Coil 1 measures a *k*-space array that, after inverse Fourier

transformation, is the true image point-wise multiplied by the sensitivity profile for coil 1. That is, $a_{1R}+ia_{1I}=(S_{1R}+iS_{1I})(v_R+iv_I)$ or $a_1=S_1v$ shown in Figure 2.7 (top right) where a_1, S_1, and v are complex scalars. Shown in Figure 2.7, the process is repeated for coil 2 (bottom right), coil 3 (bottom left), and coil 4 (top left) with the respective equations in Eq. 2.4.

$$\begin{aligned} a_{1R}+ia_{1I} &= \left(S_{1R}+iS_{1I}\right)\left(v_R+iv_I\right) \\ a_{2R}+ia_{2I} &= \left(S_{2R}+iS_{2I}\right)\left(v_R+iv_I\right) \\ a_{3R}+ia_{3I} &= \left(S_{3R}+iS_{3I}\right)\left(v_R+iv_I\right) \\ a_{4R}+ia_{4I} &= \left(S_{4R}+iS_{4I}\right)\left(v_R+iv_I\right) \end{aligned} \qquad [2.4]$$

The $n_c=4$ coil measurements create a system of equations which can be expressed as Eq. 5, which becomes the complex-valued version of Eq. 2.1. In Eq. 2.5, the *a*'s are observed, and the *S*'s and *v*'s are unobserved.

$$\begin{bmatrix} a_{1R}+ia_{1I} \\ a_{2R}+ia_{2I} \\ a_{3R}+ia_{3I} \\ a_{4R}+ia_{4I} \end{bmatrix} = \begin{bmatrix} S_{1R}+iS_{1I} \\ S_{2R}+iS_{2I} \\ S_{3R}+iS_{3I} \\ S_{4R}+iS_{4I} \end{bmatrix} \begin{bmatrix} v_R+iv_I \end{bmatrix} \qquad [2.5]$$

An equivalent representation of Eq. 2.5 is

$$\begin{bmatrix} a_{1R} \\ a_{2R} \\ a_{3R} \\ a_{4R} \\ a_{1I} \\ a_{2I} \\ a_{3I} \\ a_{4I} \end{bmatrix} = \begin{bmatrix} S_{1R} & -S_{1I} \\ S_{2R} & -S_{2I} \\ S_{3R} & -S_{3I} \\ S_{4R} & -S_{4I} \\ S_{1I} & S_{1R} \\ S_{2I} & S_{2R} \\ S_{3I} & S_{3R} \\ S_{4I} & S_{4R} \end{bmatrix} \begin{bmatrix} v_R \\ v_I \end{bmatrix} \qquad [2.6]$$

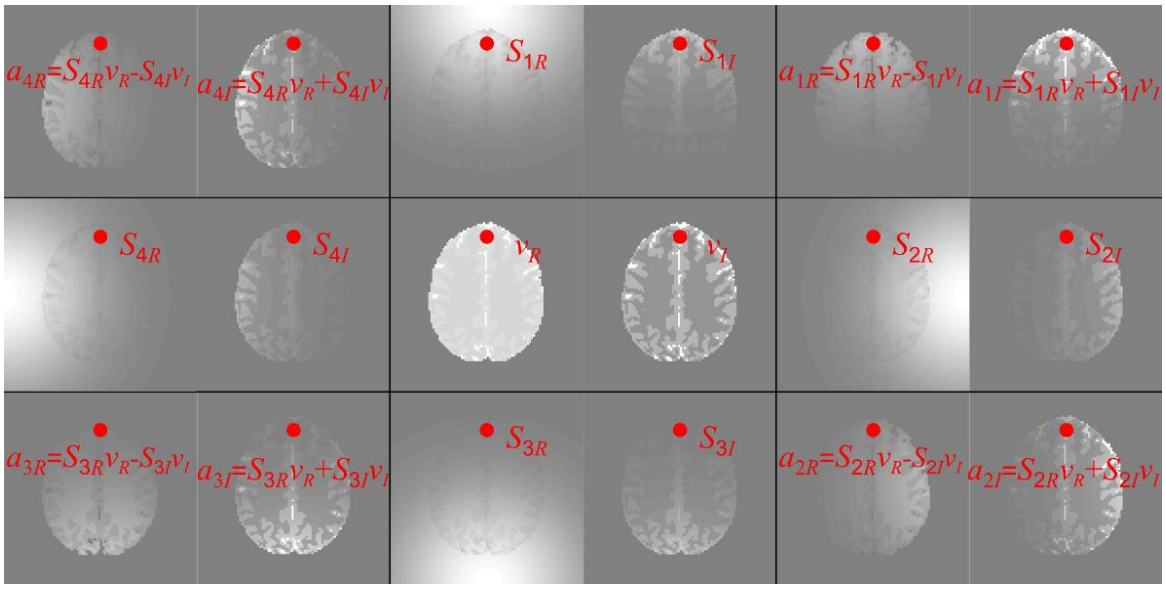

Figure 2.7: True slice complex-valued image along with complex-valued coil sensitivity profiles and complex-valued sensitivity weighted true images.

Eq. 2.5 can be more compactly written as $a = Sv$ where a is $2n_C \times 1$, S is $2n_C \times 2$, and v is 2×1. If we are able to obtain an estimate of the coil sensitivities S, we can obtain a least squares estimate of the n_A true slice voxel values v from Eq. 2.2. This process is repeated for each voxel in the image.

Since our objective is to accelerate the number of slices acquired per unit of time, we want to skip lines of the *k*-space for each image as shown in Figure 2.5 (right). Again, skipping lines in the *k*-space induces an acceleration factor. As mentioned in the previous subsection, the acceleration factor will cause the reconstructed coil images to appear as if the full image was cut into three equal horizontal strips that are summed together. This will apply to both the real and imaginary parts of the complex-valued true slice images as shown in Figure 2.8 (middle center). In Figure 2.8 (top right) the aliased image is the point-wise multiplication of the given voxel by the sensitivity profile for coil 1 summed for the three strips. The linear equations for the real component and the imaginary component are expressed in Figure 2.8 (top right). This process is repeated for coil 2 (bottom right), coil 3 (bottom left), and coil 4 (top left), displayed in Figure 2.8, with the respective real and imaginary equations.

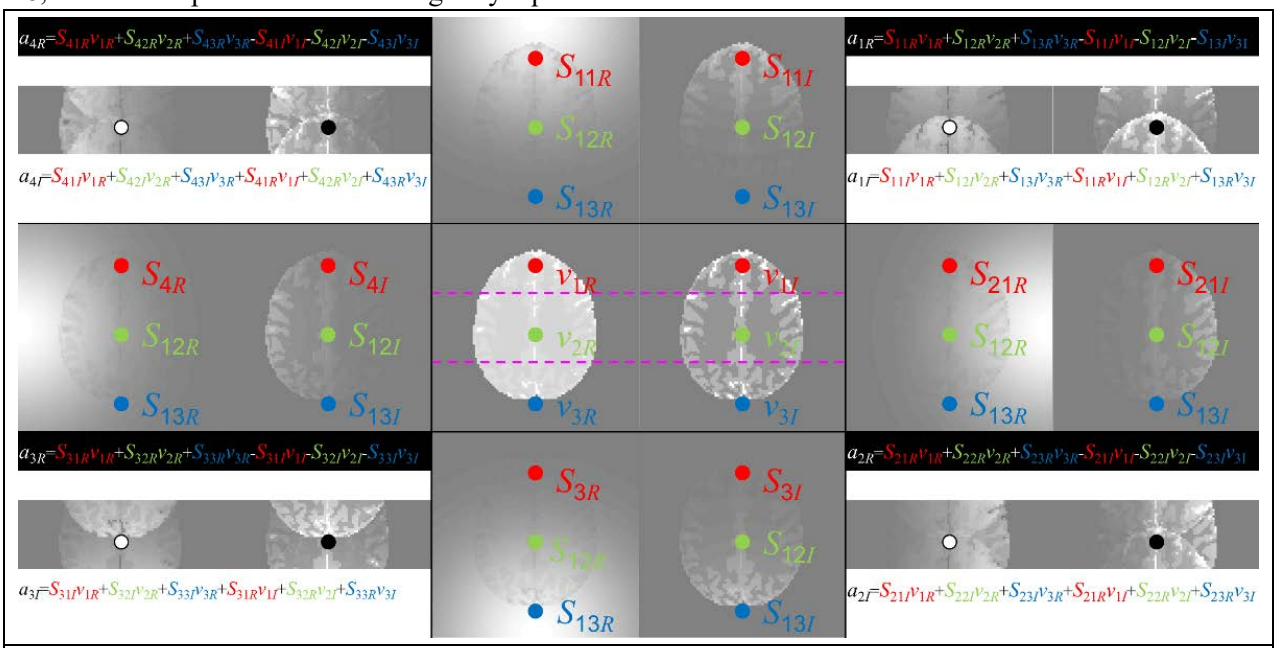

Figure 2.8: True slice image along with coil sensitivity profiles and sensitivity weighted true aliased images.

The $n_C = 4$ coil measurements create a system of equations which can be expressed in matrix form as shown in Eq. 2.7, where the *a*'s are observed coil measurements, the *S*'s are unobserved coil sensitivities, and the *v*'s are unobserved true slice voxel values.

$$\begin{bmatrix} a_{1R} \\ a_{2R} \\ a_{3R} \\ a_{4R} \\ a_{1I} \\ a_{2I} \\ a_{3I} \\ a_{4I} \end{bmatrix} = \begin{bmatrix} S_{11R} & S_{12R} & S_{13R} & -S_{11I} & -S_{12I} & -S_{13I} \\ S_{21R} & S_{22R} & S_{23R} & -S_{21I} & -S_{22I} & -S_{23I} \\ S_{31R} & S_{32R} & S_{33R} & -S_{31I} & -S_{32I} & -S_{33I} \\ S_{41R} & S_{42R} & S_{43R} & -S_{41I} & -S_{42I} & -S_{43I} \\ S_{11I} & S_{12I} & S_{13I} & S_{11R} & S_{12R} & S_{13R} \\ S_{21I} & S_{22I} & S_{23I} & S_{21R} & S_{22R} & S_{23R} \\ S_{31I} & S_{32I} & S_{33I} & S_{31R} & S_{32R} & S_{33R} \\ S_{41I} & S_{42I} & S_{43I} & S_{41R} & S_{42R} & S_{43R} \end{bmatrix} \begin{bmatrix} v_{1R} \\ v_{2R} \\ v_{3R} \\ v_{1I} \\ v_{2I} \\ v_{3I} \end{bmatrix} \quad [2.7]$$

This equation is a latent variable model similar to factor analysis but complex-valued and can be more compactly written as $a = Sv$ where a is $2n_C \times 1$, S is $2n_C \times 2n_A$, and v is $2n_A \times 1$. We can obtain a least squares estimate of the n_A true slice voxel values v from Eq. 2.2 if we are able to estimate the coil sensitivities S. This process is repeated for each voxel in the aliased image. It is important to note that $(S'S)$ is not always positive definite which can cause estimating the reconstructed voxel values to be difficult.

2.2 Bayesian Approach to SENSE (BSENSE)

For the Bayesian approach, two different models of the aliased coil measurements will be discussed. The first model will not include coil covariance between each of the coils or voxel covariance between the aliased voxels. The second model will incorporate coil covariance and aliased voxel covariance. For model one, the assumption is that there is no correlation between each of the sensitivity coils or between the voxels that were overlapping before the unaliasing of the reconstructed image. Model two will allow for potential correlation between the coils and correlation between the aliased voxels. Both models observe the aliased voxels with error. That is $a = Sv + \varepsilon$ where a is $2n_C \times 1$, S is $2n_C \times 2n_A$, v is $2n_A \times 1$, and ε is $2n_C \times 1$. The difference between the models is the assumption of the measurement error. For the first model, the error is $\varepsilon \sim N(0, \sigma^2 I_{2n_C})$, and for the second model, the error is $\varepsilon \sim N(0, I_2 \otimes \Psi)$. The Ψ is the covariance matrix for the n_C coils. The covariance matrix for the aliased voxels Υ in model 2 is analyzed in the prior distributions of the sensitivity coils $\boldsymbol{S}$ and the unobserved voxel values v. Two different representations of the coil sensitivities will be used. In the first S is $2n_C \times 2n_A$ as presented in Eq. 2.7 is necessary for the proper representation of complex-valued multiplication while in the second $\boldsymbol{S}$ is $n_C \times 2n_A$ as shown in Eq. 2.12 so as to only place a prior distribution on each element once. The second representation ensures the proper skew symmetry of the *a posteriori* estimated sensitivities.

2.2.1 Model One: Data Likelihood, Prior and Posterior Distributions

The likelihood distribution for the measurements become

$$P(a \mid S, v, \sigma^2) \propto (\sigma^2)^{-\frac{2n_C}{2}} \exp\left[-\frac{1}{2\sigma^2}(a - Sv)'(a - Sv) \right] \quad [2.8]$$

where a is the observed aliased coil image measurements, S is the unobserved coil reception sensitivities, v is the unobserved true image slice voxel values, and σ^2 is the unobserved image noise variance.

From the likelihood distribution, we can quantify available prior information about the unobserved parameters S, v, and σ^2 with assessed hyperparameters of prior distributions. The coil sensitivities S represented as $\boldsymbol{S}$ and the voxel values v are specified to have normal distributions and the noise variance σ^2 is specified to have an inverse gamma distribution i.e.,

$$P(\boldsymbol{S} \mid n_S, \boldsymbol{S}_0, \sigma^2) \propto (\sigma^2)^{-\frac{2n_C n_A}{2}} \exp\left[-\frac{n_S}{2\sigma^2} tr[(\boldsymbol{S} - \boldsymbol{S}_0)'(\boldsymbol{S} - \boldsymbol{S}_0)] \right] \quad [2.9]$$

$$P(v \mid n_v, v_0, \sigma^2) \propto (\sigma^2)^{-\frac{2n_A}{2}} \exp\left[-\frac{n_v}{2\sigma^2}(v - v_0)'(v - v_0) \right] \quad [2.10]$$

$$P(\sigma^2 \mid \alpha, \beta) \propto (\sigma^2)^{-(\alpha+1)} \exp\left[-\frac{\beta}{\sigma^2} \right] \quad [2.11]$$

with hyperparameters n_S, $\boldsymbol{S}_0$, n_v, v_0, α, and β to be assessed from the initial calibrated images. In Eq. 2.9, $\boldsymbol{S}$ is $n_C \times 2n_A$ as expressed in Eq. 2.12

$$\boldsymbol{S} = \begin{bmatrix} \boldsymbol{S}_{11R} & \boldsymbol{S}_{12R} & \boldsymbol{S}_{13R} & \boldsymbol{S}_{11I} & \boldsymbol{S}_{12I} & \boldsymbol{S}_{13I} \\ \boldsymbol{S}_{21R} & \boldsymbol{S}_{22R} & \boldsymbol{S}_{23R} & \boldsymbol{S}_{21I} & \boldsymbol{S}_{22I} & \boldsymbol{S}_{23I} \\ \boldsymbol{S}_{31R} & \boldsymbol{S}_{32R} & \boldsymbol{S}_{33R} & \boldsymbol{S}_{31I} & \boldsymbol{S}_{32I} & \boldsymbol{S}_{33I} \\ \boldsymbol{S}_{41R} & \boldsymbol{S}_{42R} & \boldsymbol{S}_{43R} & \boldsymbol{S}_{41I} & \boldsymbol{S}_{42I} & \boldsymbol{S}_{43I} \end{bmatrix} \quad [2.12]$$

By combining the likelihood distribution and the prior distributions, the posterior distribution of the coil sensitivities S (or $\boldsymbol{S}$), the true slice voxel values v, and the noise variance σ^2 is

$$P(\boldsymbol{S}, v, \sigma^2 \mid a) \propto P(a \mid S, v, \sigma^2) P(\boldsymbol{S} \mid n_S, \boldsymbol{S}_0, \sigma^2) P(v \mid n_v, v_0, \sigma^2) P(\sigma^2 \mid \alpha, \beta) \quad [2.13]$$

with the distributions specified from Equations 2.10, 2.11, 2.12, and 2.13.

2.2.2 Model One: Parameter Estimation

Using the posterior distribution in Eq. 2.13 with the priors described in Equations 2.9, 2.10, and 2.11 along with the likelihood distribution in Eq. 2.8, two techniques are used to estimate the unobserved parameters S, v, and σ^2: Maximum A Posteriori (MAP) estimation using the Iterated Conditional Modes (ICM) optimization algorithm (Lindley and Smith, 1972) and a Markov Chain Monte Carlo (MCMC) Gibbs sampler (Geman and Geman, 1984). Starting with initial estimates of each parameter, ICM iterates over the parameters calculating its conditional mode, and converges to a local maximum of the joint posterior density. The modes for the parameters for the MAP estimates using the ICM algorithm are

$$\hat{S} = (av' + n_S S_0)(vv' + n_S I_{2n_A})^{-1} \quad [2.14]$$

$$\hat{v} = (S'S + n_v I_{2n_A})^{-1}(S'a + n_v v_0) \quad [2.15]$$

$$\hat{\sigma}^2 = \frac{(a - Sv)'(a - Sv) + n_v (v - v_0)'(v - v_0) + \alpha\beta + n_S tr[(S - S_0)(S - S_0)]}{2(2n_c + 2n_A + \alpha + 2n_c n_A + 1)} \quad [2.16]$$

It can be shown that the full conditional distributions of each parameter S, v, and σ^2 for the MCMC Gibbs sampler are given by

$$v \mid S, \sigma^2, a \sim N(\hat{v} = (S'S + n_v I_{2n_A})^{-1}(S'a + n_v v_0), \sigma^2 (S'S + n_v I_{2n_A})^{-1}) \quad [2.17]$$

$$\boldsymbol{S} \mid v, \sigma^2, a \sim MN(\hat{\boldsymbol{S}} = (\boldsymbol{a}'C' + n_S \boldsymbol{S}_0)(CC' + n_S I_{2n_A})^{-1}, I_{n_c}, (CC' + n_S I_{2n_A})^{-1}) \quad [2.18]$$

$$\sigma^2 \mid v, S, a \sim IG(\alpha_*, \beta_*) \quad [2.19]$$

where C is $2n_A \times 2$ voxel values as expressed in Eq. 2.20, $\alpha_* = n_C n_A + n_C + n_A \alpha$, $\beta_* = 0.5[(a - Sv)'(a - Sv) + n_v (v - v_0)'(v - v_0) + n_S tr((\boldsymbol{S} - \boldsymbol{S}_0)(\boldsymbol{S} - \boldsymbol{S}_0)') + 2\beta]$, and $\boldsymbol{a}$ is $n_C \times 2$ observed coil measurements having the real part in the first column and the imaginary part in the second column as such $[a_R, a_I]$.

$$C = \begin{bmatrix} v_{1R} & v_{1I} \\ v_{2R} & v_{2I} \\ v_{3R} & v_{3I} \\ -v_{1I} & v_{1R} \\ -v_{2I} & v_{2R} \\ -v_{3I} & v_{3R} \end{bmatrix} \quad [2.20]$$

The Gibbs sampler begins with initial values for $\boldsymbol{S}$ and v.

2.2.3 Model Two: Data Likelihood, Prior and Posterior Distributions

The data likelihood for the second model becomes

$$P(a \mid S, v, \Psi) \propto |\Psi|^{-\frac{2}{2}} \exp\left[-\frac{1}{2}(a - Sv)'(I_2 \otimes \Psi)^{-1}(a - Sv) \right] \quad [2.21]$$

where a is the observed aliased coil image measurements, S is the unobserved coil reception sensitivities, v is the unobserved true slice image voxel values, and Ψ is the unobserved coil covariance. With this model, we specify that the coil covariance is the same for real part and the imaginary part with no correlation between the real and imaginary parts. In SENSE image reconstruction (Pruessmann et al., 1999), when Ψ is estimated from complex-valued data, the covariance matrix is reformatted such that the real part and imaginary part have the same covariance structure. For cross-dependency, we will work under the assumption that there is no correlation between the real and imaginary parts.

Along with induced coil covariance in the data likelihood distribution, coil covariance must also be incorporated in the prior distribution of the coil sensitivities $\boldsymbol{S}$. Pruessmann et al. clarifies that unfolding can cause artifacts in the final reconstructed image which means there is potential covariance between the aliased voxels from the unaliasing process. In Figure 2.8 (middle center) shows three voxels (red, blue, and green circles) that are in a particular column and the same row of each of the strips. When the strips are folded together, those three voxels will be in the same row and column in the aliased images. Once the image is reconstructed and unfolded, there could be an induced correlation between those three voxels from the unaliasing process. This voxel covariance becomes an unobserved parameter that needs to be estimated. The prior distributions incorporating both coil covariance and voxel covariance are

$$P(v \mid v_0, \Upsilon) \propto |\Upsilon|^{-\frac{2}{2}} \exp\left[-\frac{1}{2}(v - v_0)'(I_2 \otimes \Upsilon)(v - v_0) \right] \quad [2.22]$$

$$P(\boldsymbol{S} \mid \boldsymbol{S}_0, \Psi, \Upsilon) \propto |\Psi|^{-\frac{2n_A}{2}} |\Upsilon|^{-\frac{n_c}{2}} \exp\left[-\frac{1}{2} tr\left[\Psi^{-1}(\boldsymbol{S} - \boldsymbol{S}_0)(I_2 \otimes \Upsilon^{-1})(\boldsymbol{S} - \boldsymbol{S}_0)' \right] \right] \quad [2.23]$$

$$P(\Upsilon \mid \nu_1, \Gamma) \propto |\Upsilon|^{-\frac{\nu_1 + n_A + 1}{2}} \exp\left[-\frac{1}{2} tr\left(\Upsilon^{-1}\Gamma \right) \right] \quad [2.24]$$

$$P(\Psi \mid \nu_2, \Delta) \propto |\Psi|^{-\frac{\nu_2 + n_c + 1}{2}} \exp\left[-\frac{1}{2} tr\left(\Psi^{-1}\Delta \right) \right] \quad [2.25]$$

where v is $2n_A \times 1$, $\boldsymbol{S}$ is $n_c \times 2n_A$, Υ is $n_A \times n_A$, and Ψ is $n_C \times n_C$ and hyperparameters $\boldsymbol{S}_0$, v_0, ν_1, and ν_2 to be assessed from initial calibration images.

By combining the likelihood distribution and the prior distributions, the posterior distribution of the coil sensitivities S, the true slice voxel values v, the voxel covariance Υ, and the coil covariance Ψ is

$$P(\boldsymbol{S}, v, \Upsilon, \Psi \mid a) \propto P(a \mid S, v, \Psi) P(v \mid v_0, \Upsilon) P(\boldsymbol{S} \mid \boldsymbol{S}_0, \Psi, \Upsilon) P(\Upsilon \mid \nu_1, \Gamma) P(\Psi \mid \nu_2, \Delta) \quad [2.26]$$

with the distributions specified from Equations 2.21, 2.22, 2.23, 2.24, and 2.25.

2.2.4 Model Two: Parameter Estimation

Using the posterior distribution in Eq. 2.26 with the priors described in Equations 2.22, 2.23, 2.24, and 2.25, and the likelihood distribution in Eq. 2.21, a Gibbs sampler is used to estimate the unobserved parameters S, v, Υ, Ψ. It can be shown that the full conditional distributions of each parameter S, v, Υ, Ψ are given in Equations 2.27, 2.28, 2.29, and 2.30.

$$v \mid a, S, v_0, \Upsilon, \Psi \sim N(\hat{v} = (S'(I_2 \otimes \Psi^{-1})S + I_2 \otimes \Upsilon^{-1})^{-1}(S'(I_2 \otimes \Psi^{-1})a + (I_2 \otimes \Upsilon^{-1})v_0), \\ (S'(I_2 \otimes \Psi^{-1})S + (I_2 \otimes \Upsilon^{-1})^{-1}) \quad [2.27]$$

$$h \mid a, v, S_0, \Upsilon, \Psi \sim N(\hat{h}, \Psi \otimes (CC' + I_2 \otimes \Upsilon^{-1})) \quad [2.28]$$

$$\Upsilon \mid a, v, S, \Psi \sim IW(\nu_\Upsilon, \Omega_\Upsilon) \quad [2.29]$$

$$\Psi \mid a, v, S, \Upsilon \sim IW(\nu_\Psi, \Omega_\Psi) \quad [2.30]$$

where Υ and Ψ follow inverse Wishart distributions, $h = vec(\boldsymbol{S})$, $h = vec(\boldsymbol{S})$ where $\boldsymbol{S} = (\boldsymbol{a}'C' + \boldsymbol{S}_0(I_2 \otimes \Upsilon^{-1}))(CC' + I_2 \otimes \Upsilon^{-1})^{-1}$, $\Omega_\Upsilon = (v - v_0)(v - v_0)' + (S - S_0)'(I_2 \otimes \Psi^{-1})(S - S_0) + \Gamma$, $\nu_\Upsilon = \nu_1 + n_A + 2$, $\nu_\Psi = \nu_2 + n_C + n_A + 2$, $\Omega_\Psi = (\boldsymbol{a} - \boldsymbol{S}B)(\boldsymbol{a} - \boldsymbol{S}B)' + (\boldsymbol{S} - \boldsymbol{S}_0)(I_2 \otimes \Upsilon^{-1})(\boldsymbol{S} - \boldsymbol{S}_0)' + \Delta$, X is $2n_C \times n_A$ where the real part of $\boldsymbol{S}$ is stacked on top of the imaginary part, and B is $2n_A \times 2$ voxel values as expressed in Eq. 2.31

$$\tilde{B} = \begin{bmatrix} v_{1R} & 0 \\ v_{2R} & 0 \\ v_{3R} & 0 \\ 0 & v_{1I} \\ 0 & v_{2I} \\ 0 & v_{3I} \end{bmatrix} \quad [2.31]$$

The Gibbs sampler begins with initial values for $\boldsymbol{S}$, v, and Ψ.

3. Simulated Single Slice Image Results

3.1 Hyperparameter Assessment

Prior to an fMRI experiment, a short non-task based set of $n_{cal} = 30$ full *k*-space volume images for the n_C coils can be obtained similar to Figure 2.7. These "calibration" images can be utilized to assess the hyperparameters of the prior distributions for the parameters. These n_{cal} calibration images can be averaged as in Figure 3.1. The root sum of squares in each voxel is computed from these $n_C = 4$ complex-valued coil images for an initial magnitude v_{0M} of the prior mean as in Eq. 3.1.

$$v_{0M} = \left[a_{R1}^2 + a_{1I}^2 + a_{2R}^2 + a_{2I}^2 + a_{3R}^2 + a_{3I}^2 + a_{4R}^2 + a_{4I}^2 \right]^{1/2} \quad [3.1]$$

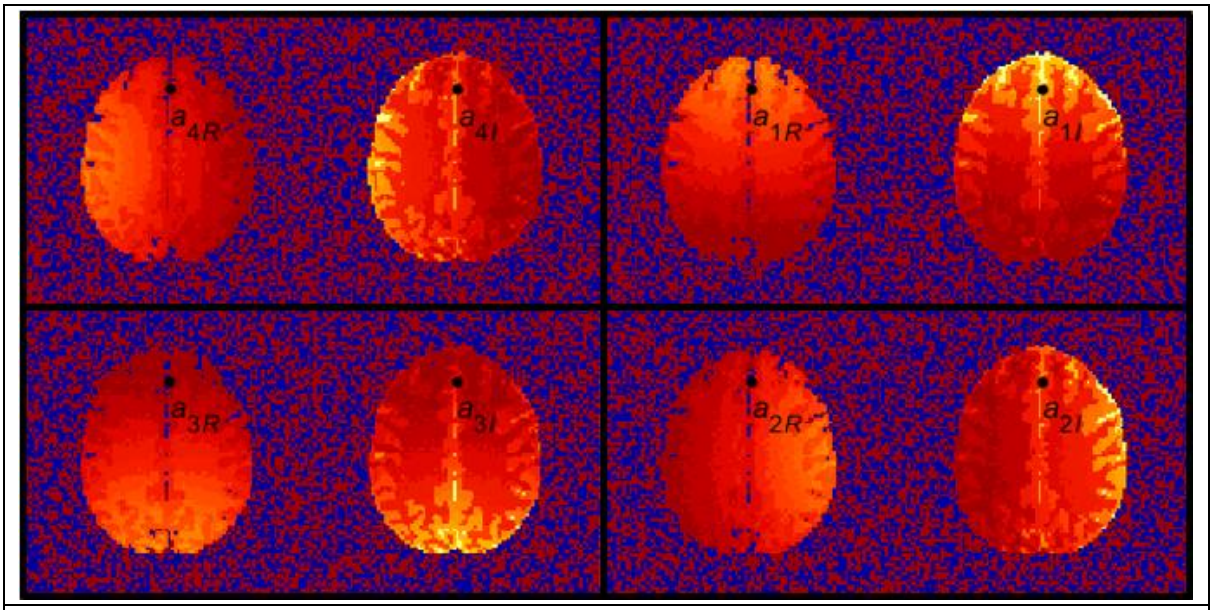

Figure 3.1: Average of m real and imaginary calibration images for the N_C coils.

Due to the nonuniform coil coverage, an adjustment must be made to the center of the image. The initial prior mean magnitude in Figure 3.2 (left) is pointwise multiplied (Hadamard product, $\odot$) by a Gaussian hill, as expressed in Eq. 3.2 and shown in Figure 3.2 (middle), to account for this nonuniformity as in Figure 3.2 (right) for a revised v_{0M} .

$$h(x,y) = 1.1 + .4 \times \exp\left\{ -\frac{1}{2n_{xy}} \left[(x - n_{xy}/2 - 1)^2 + (y - n_{xy}/2 - 1)^2 \right] \right\} \qquad [3.2]$$

In Eq. 3.2, n_{xy} equals number of rows or the number of columns in the image.

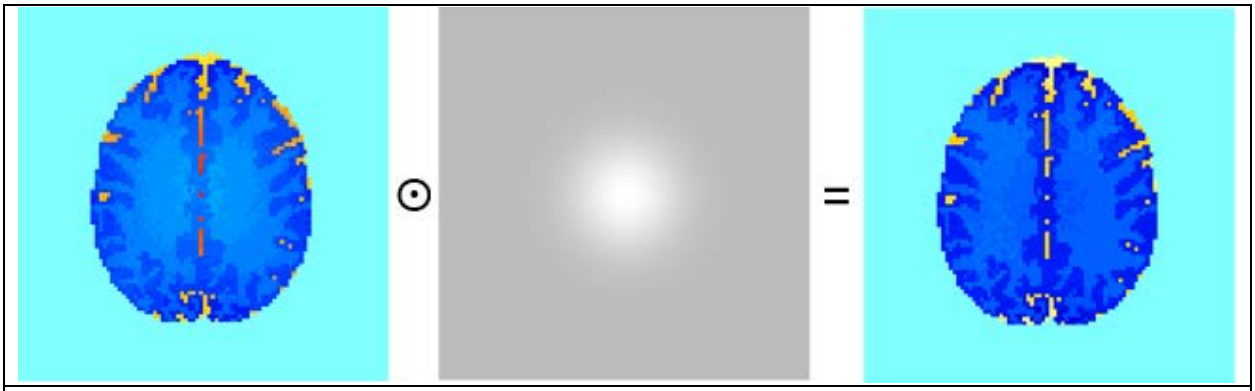

Figure 3.2: Point-wise adjustment for the magnitude of the prior voxel mean image.

The n_c complex-valued averaged calibration images in Figure 3.1 are pointwise divided by the magnitude of the prior mean in Figure 3.2 (right) in order to arrive at the prior mean for the real-imaginary coil sensitivities in Figure 3.3 (top section) with magnitude-phase in Figure 3.3 (bottom section). The hyperparameters n_S and n_v were set to be the number of calibration images

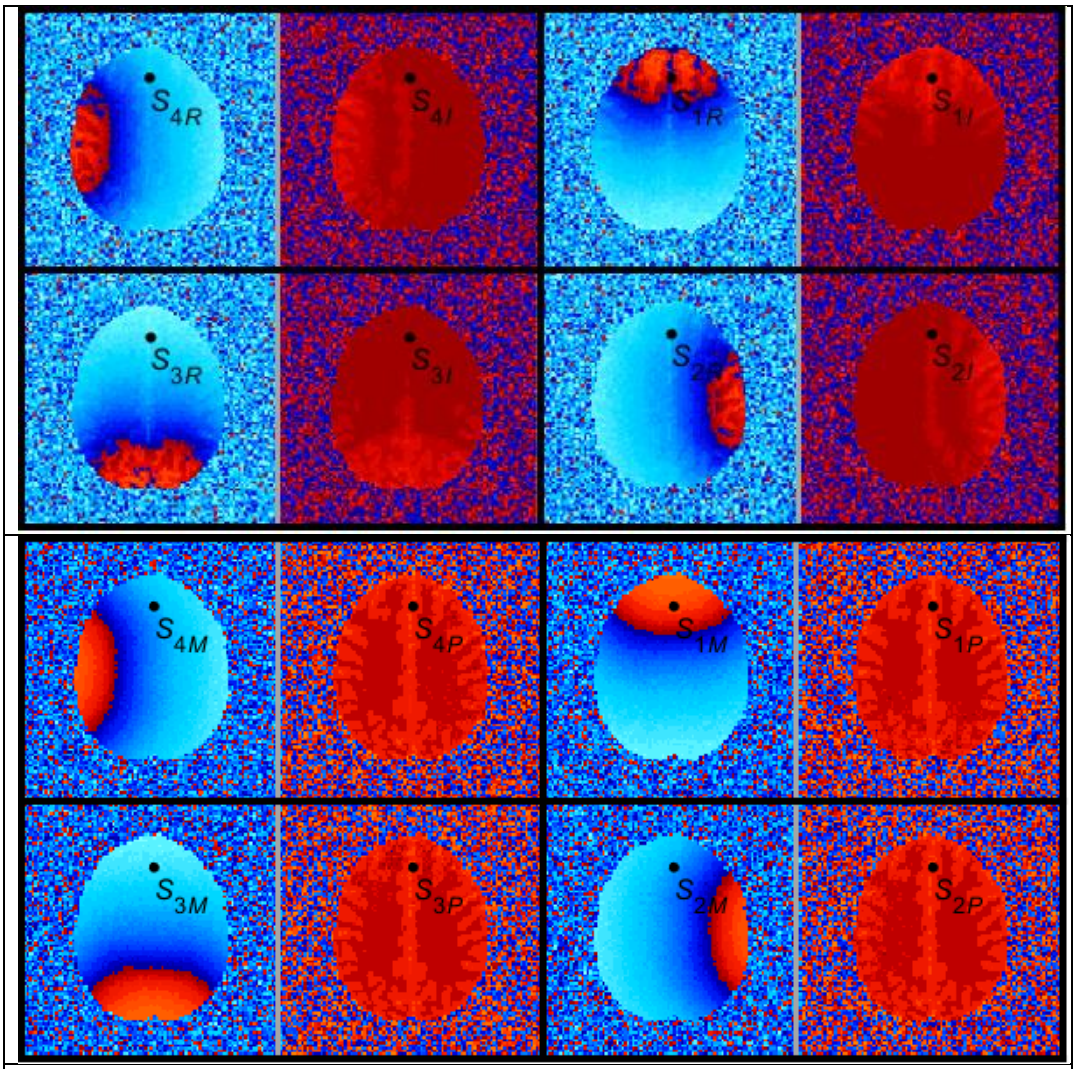

Figure 3.3: Prior mean for coil sensitivities.

$n_{cal} = 30$. The average residual variance over the voxels of the calibration images was evaluated to be $\sigma_0^2 = 1.005$. The α hyperparameter was set to be $\alpha = (n_{cal} - 1)$ and β to be $\beta = (n_{cal} - 1)$ for simplicity reasons. Bruce (13) evaluated an estimate for coil covariance Ψ which was used as an initial estimate for this research.

3.2 Posterior Unaliased Image Results for Model One

A single image was generated for $n_C = 4$ coils by adding $N(0, \sigma^2)$ noise to the noiseless coil images in Figure 2.8. The derived aliased noisy coil images are shown in Figure 3.4 and used to demonstrate the use of BSENSE. Figure 3.5 displays the true magnitude, phase, real part, and imaginary part of the image.

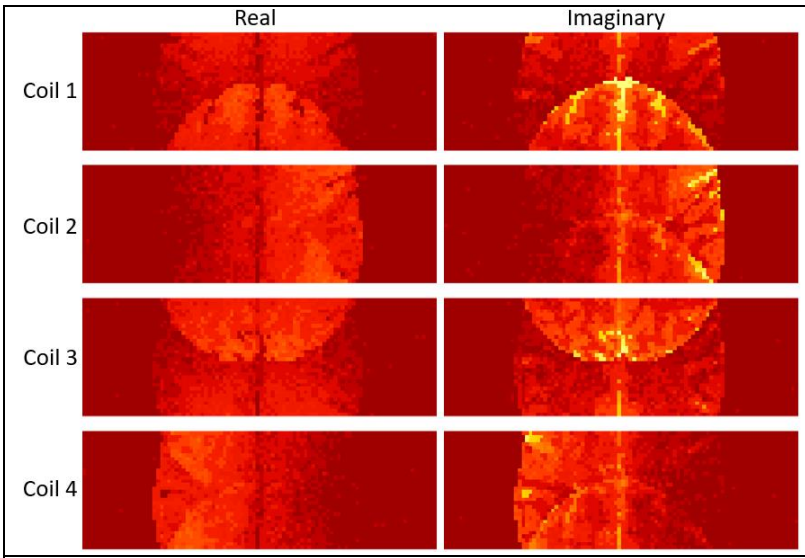

Figure 3.4: Simulated observed noisy coil images for one time point in an fMRI experiment.

Using the observed aliased coil images in Figure 3.4, the model that does not incorporate coil covariance or voxel covariance, and the associated hyperparameters, the MAP BSENSE unaliased images were estimated using ICM and displayed in Figure 3.6.

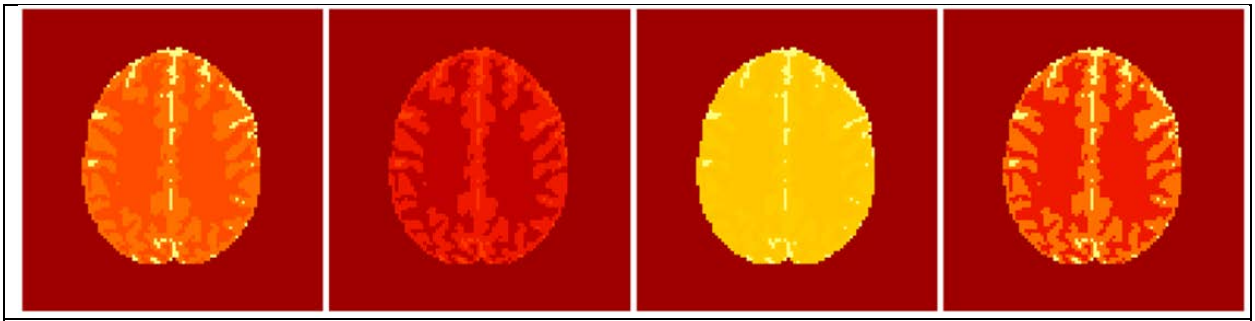

Figure 3.5: The true images magnitude (left), phase (left middle), real part (right middle), and imaginary part (right)

For the MCMC Gibbs sampling technique, the total number of iterations used was $L = 10,000$ with a $burn = 2500$. The initial values for $\boldsymbol{S}$ and ν were used to generate a σ^2 value, initializing the Gibbs sampler. This technique, again, used the observed aliased coil images in Figure 3.4, the first model, and the associated hyperparameters to estimate the voxel values for the image reconstruction. The estimated voxel

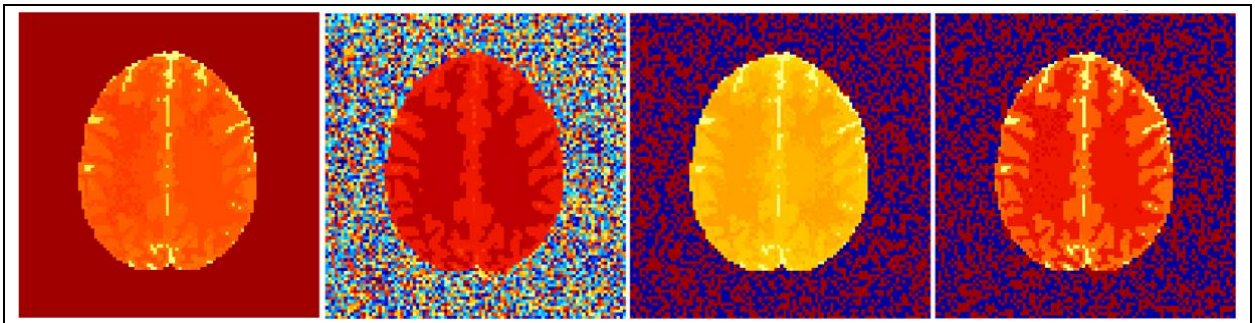

Figure 3.6: MAP BSENSE unaliased images magnitude (left), phase (left middle), real part (right middle), and imaginary part (right)

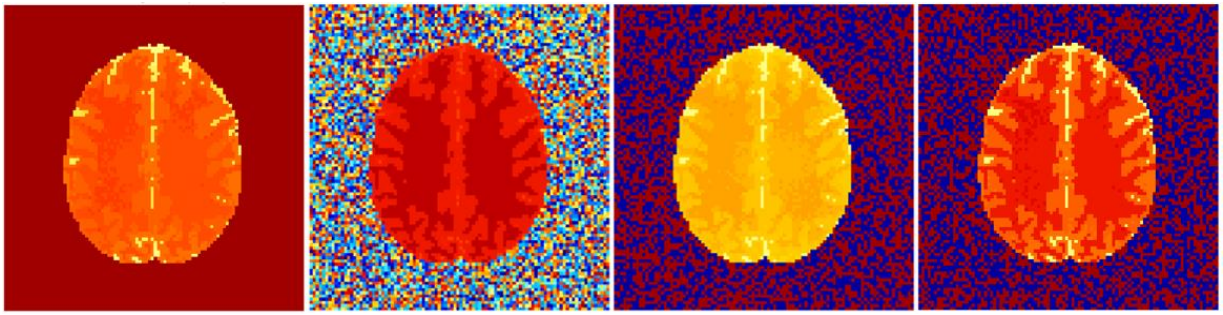

Figure 3.7: MCMC Gibbs sampling BSENSE unaliased mean images with no induced coil and aliased voxel correlations with magnitude (left), phase (left middle), real part (right middle), and imaginary part (right)

values v of the last $M = 7500$ iterations in the Gibbs sampler were averaged and unaliased to form the images shown in Figure 3.7. The reconstructed images appear to be very similar to the true image slice.

We can see that the MAP estimates using the ICM algorithm and the MCMC Gibbs sampler for BSENSE image reconstruction produces similar outputs with each other, providing images with no aliasing artifacts. Along with taking the means of the voxels, the Gibbs sampling algorithm also allows us to look at the variances of the voxels. Calculating the variance of the voxels follows the same process as calculating the mean of the voxel values. The variance of each voxel is calculated using the last $M = 7500$ iterations of the Gibbs sampler with the variance images displayed in Figure 3.8.

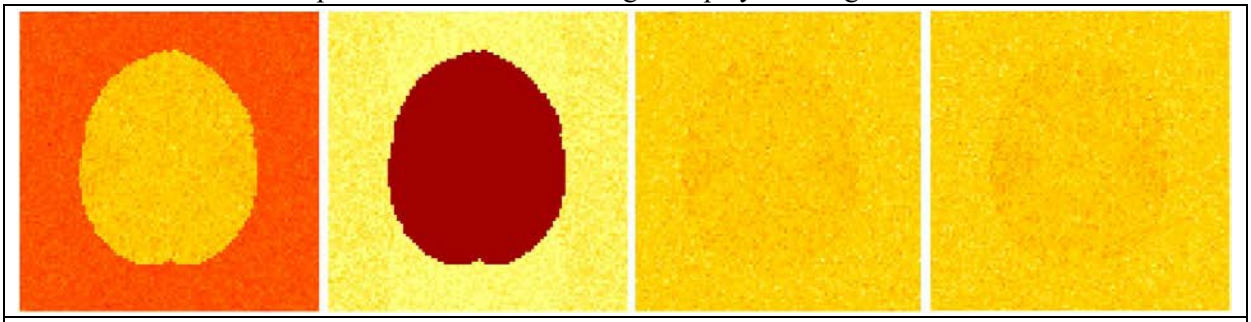

Figure 3.8: MCMC Gibbs sampling BSENSE unaliased variance images with magnitude on the left, phase in the middle left, real in in the middle right, and imaginary on the right.

The magnitude (left), real (middle right), and imaginary (right) variance images are scaled from 0 to 0.05 and the phase (middle left) variance image is scaled from 0 to 1. The lighter the color in the images in Figure 3.8, the higher the variance. The variance of the magnitude in Figure 3.8 shows that it is dependent on whether the voxel is inside the brain. It also indicates low voxel variance which narrows the statistical deviation of the estimated voxel value from the Gibbs sampling technique. The low phase variance inside the brain indicates little change between the angles of the voxels in the Gibbs sampler.

The process of the BSENSE image reconstruction could naturally induce a correlation within the voxels that are aliased together and the MCMC Gibbs sampler allows for correlation analysis. Figure 3.9 exhibits an example of the three voxels that were unaliased and the correlation associated with those voxels. The correlation between the voxels is computed by using Eq 3.3

$$corr(v_i, v_j) = \frac{\text{cov}(v_i, v_j)}{\sigma_i \sigma_j} \qquad [3.3]$$

where $\text{cov}(v_i, v_j)$ is the covariance between voxel i and voxel j, σ_i is the standard deviation for voxel i, σ_j is the standard deviation for voxel j, and $i \neq j$. Like mean and variance, the last

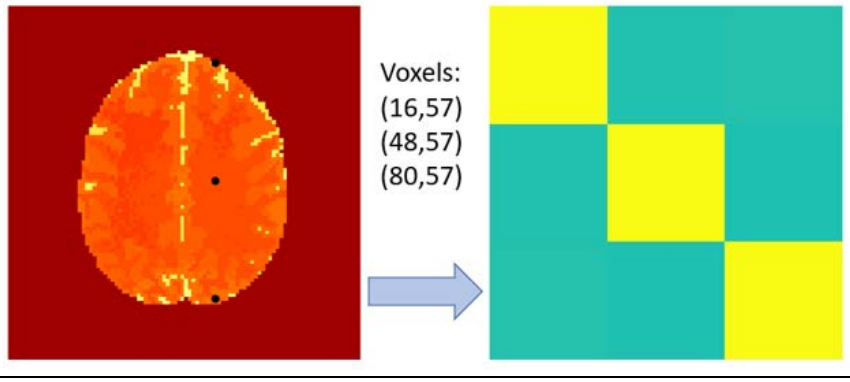

Figure 3.9: Correlation between three overlapping voxels

$M = 7500$ iterations of the Gibbs sampler are used to calculate correlation. The correlation between the voxels in Figure 3.9 appears to be low (close to zero). In Figure 3.10, we can see the correlation matrix of every voxel with the other voxels and the further shows the low correlation between the voxels. The largest absolute correlation between two voxels off the diagonal was

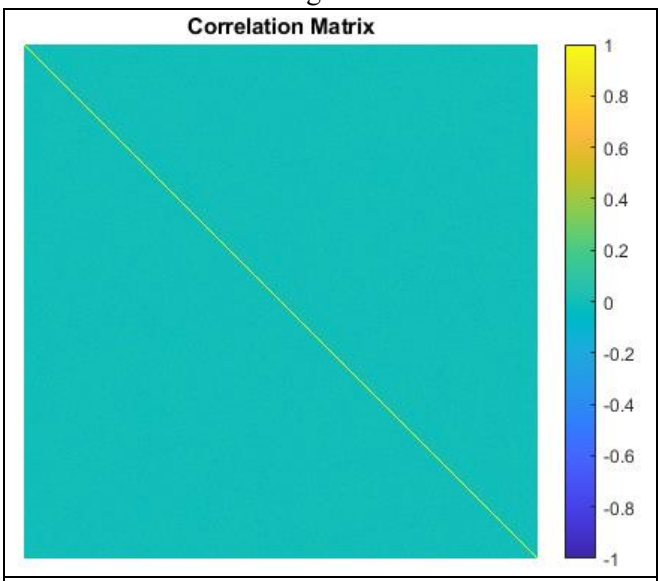

Figure 3.10: Correlation matrix of all voxels

calculated to be 0.0883 indicating no correlation between the aliased voxels which will reduce any risk of non-biological artifacts from our images. Even though we have results that indicate no correlation between the aliased voxels, we still need to incorporate the second model so it can capture any potential correlation that the first model ignores.

3.3 Posterior Unaliased Image Results for Model Two

A single slice was generated for $n_C = 4$ coils by adding $N(0, I_2 \otimes \Psi^{-1})$ noise that incorporates coil covariance to the noiseless coil images in Figure 2.8. The derived aliased noisy coil images are shown in Figure 3.11 and used to demonstrate the use of BSENSE.

Again, Figure 3.5 displays the images of the true image's magnitude, phase, real part, and imaginary part. For this model that accounts for possible correlation between each coil and between the aliased voxels,

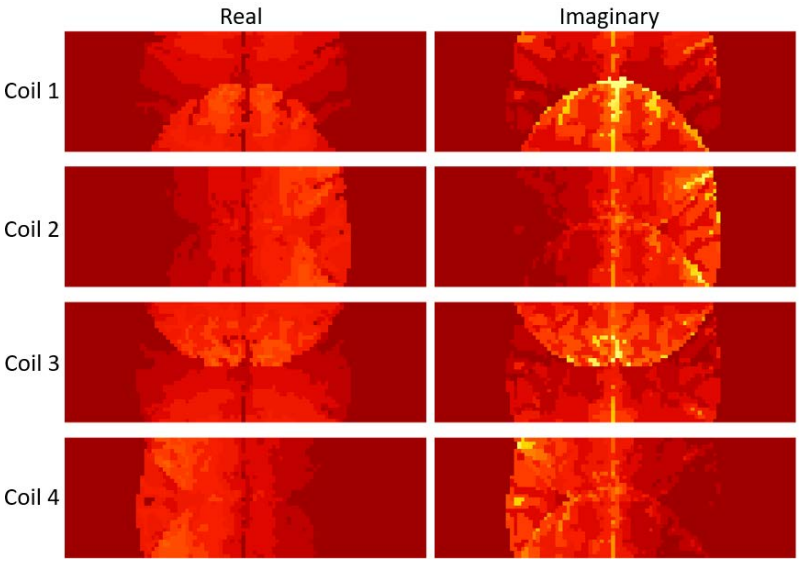

Figure 3.11: Simulated observed noisy coil images with incorporated coil covariance for one time point in an fMRI experiment.

Gibbs sampling will be utilized. The total number of iterations used was $L = 10,000$ with a $burn = 2500$. This technique used the observed aliased coil images in Figure 3.11, the second Bayesian model, and the respective hyperparameters to estimate the voxel values for the final reconstructed image. The estimated voxel values v of the last $M = 7500$ iterations in the Gibbs sampler were averaged. The reconstructed images, shown in Figure 3.12, appear to have no aliasing artifacts and look similar to the true image slice.

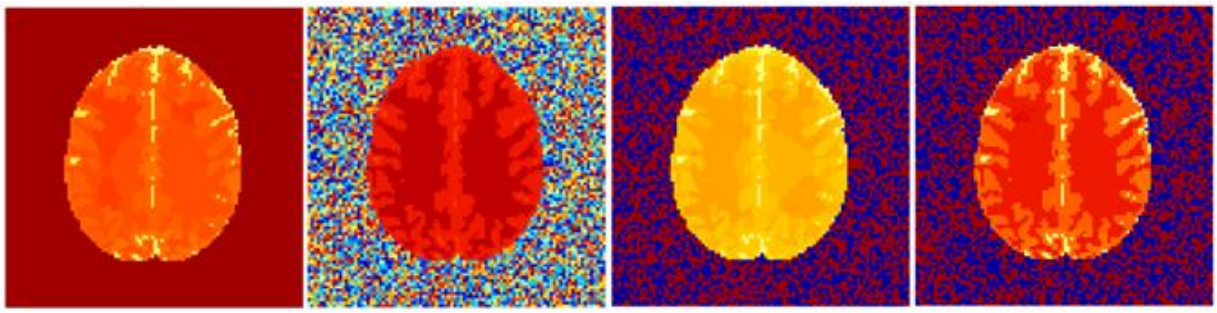

Figure 3.12: MCMC Gibbs sampling BSENSE unaliased mean images including induced coil and aliased voxel correlations with magnitude (left), phase (left middle), real part (right middle), and imaginary part (right)

Calculating the variance of the voxels follows the same process as calculating the mean of the voxel values. The variance of each voxel is calculated using the last $M = 7500$ iterations in the Gibbs sampler and illustration of the variance images are shown in Figure 3.13.

Just like in Figure 3.8, the magnitude (left), real (middle right), and imaginary (right) variance images are scaled from 0 to 0.05 and the phase (middle left) variance image is scaled from 0 to 1 with the lighter colors indicating higher variance. The magnitude variance image in Figure 3.13 (left), the variance of the voxel is location dependent in the aliased image, like model one results. The voxels inside the brain appear to have a slightly higher variance than those outside the brain.

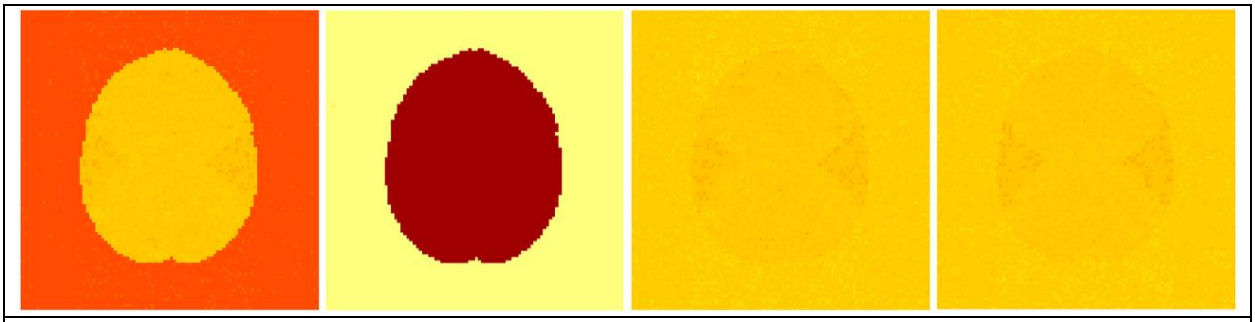

Figure 3.13: MCMC Gibbs sampling BSENSE unaliased variance images with magnitude on the left, phase in the middle left, real in in the middle right, and imaginary on the right.

In Figure 3.14, we can see the 9216×9216 correlation matrix of between every voxel of the final reconstructed image The largest absolute correlation between two voxels off the diagonal was calculated to be 0.0933 in the correlation matrix on the left in Figure 3.14. Even with incorporating aliased voxel covariance and coil covariance into our model, the results still showed no correlation from unaliasing the voxels. This outcome reduces the risk of having non-biological correlation in the fMRI results which is otherwise seen in SENSE image reconstruction (Bruce, 2014).

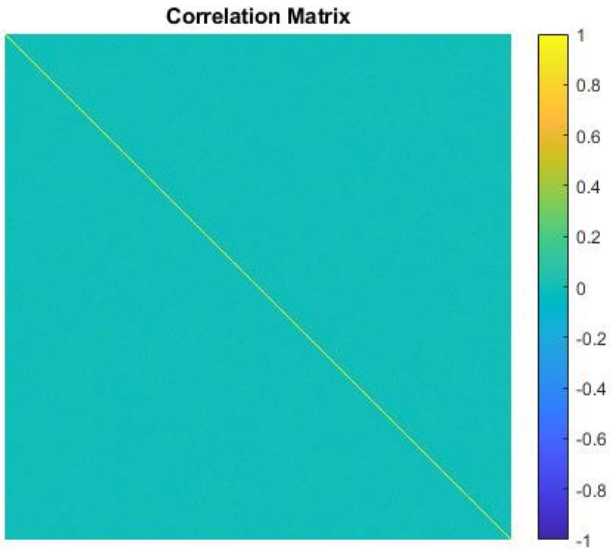

Figure 3.14: Correlation matrix of all voxels

4. Series of Simulated Slice Images Results

4.1 Series of Posterior Unaliased Images Using Model One

In MRI, there will not simply be one single image that will need to be reconstructed. There will be a volume of images that can contain hundreds of slices so BSENSE will need to reconstruct a series of slices. For the simulated series of images, $n_{IM} = 4$ images were generated for $n_C = 4$ coils by adding $N(0, \sigma^2)$ noise, where $\sigma^2 = 1$, to the noiseless coil images in Figure 2.8. The derived aliased noisy coil images are shown in Figure 4.1 and used to demonstrate the use of BSENSE for a series of images.

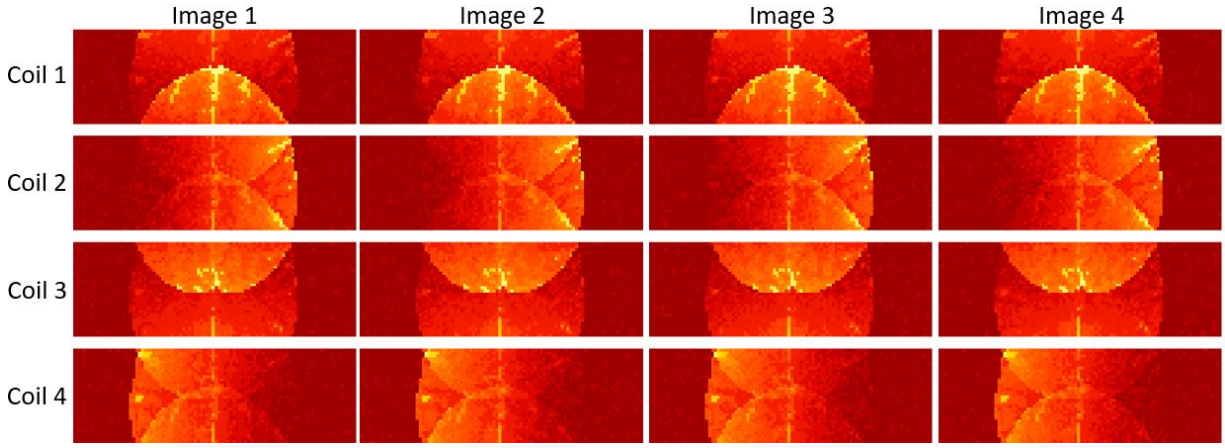

Figure 4.1: Simulated observed noisy magnitude coil images without incorporated coil covariance for a series of four images

For the series of images, the MCMC Gibbs sampling technique will be utilized. The total number of iterations used was $L = 1000$ with a $burn = 200$. The voxel values for the reconstructed images were estimated using the first model, its associated hyperparameters, and the observed aliased coil images in Figure 4.1. The last $M = 800$ voxel values in the Gibbs sampler were averaged together and unaliased to form the magnitude images shown in Figure 4.2.

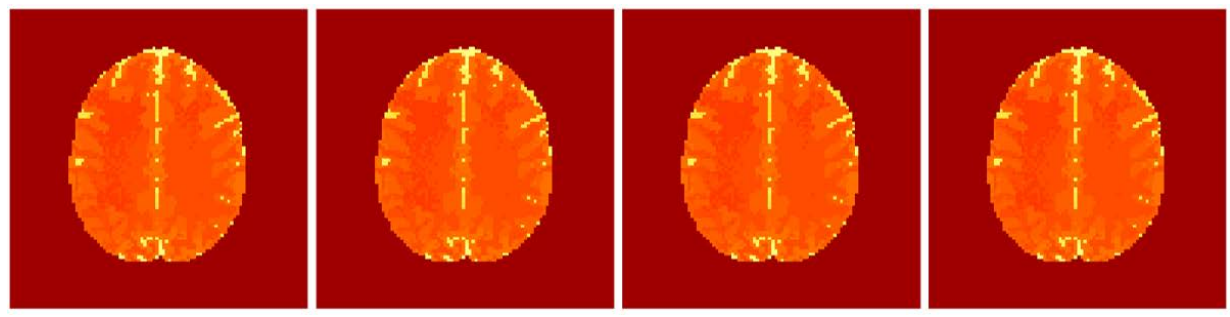

Figure 4.2: MCMC Gibbs sampling BSENSE series of $n_{IMG} = 4$ unaliased magnitude mean images that does not include the induced coil and aliased voxel covariances.

This shows a successful reconstruction of a series of $n_{IM} = 4$ images. The number of images in the series can be changed, and this process can be repeated with a larger number of images which can be used to create a volume of images. Figure 4.3 displays the magnitude variance images for
for the $n_{IM} = 4$ images in the series. Calculating the variances of the voxels follows the same process discussed in the previous section. The variance of each voxel is calculated using the last $M = 800$ iterations

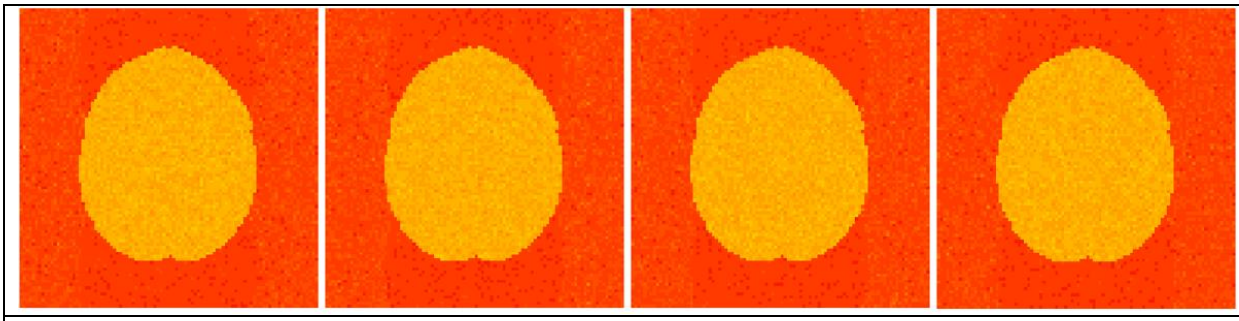

Figure 4.3: MCMC Gibbs sampling BSENSE series of $n_{IMG} = 4$ unaliased magnitude variance images.

in the Gibbs sampler. These magnitude variance images show low voxel variance, similar to the results from the single slice image.

4.2 Series of Posterior Unaliased Images Using Model Two

The process from the previous subsection is repeated but instead we will use the second model. For the simulated series of images, $n_{IM} = 4$ images were generated for $n_C = 4$ coils by adding

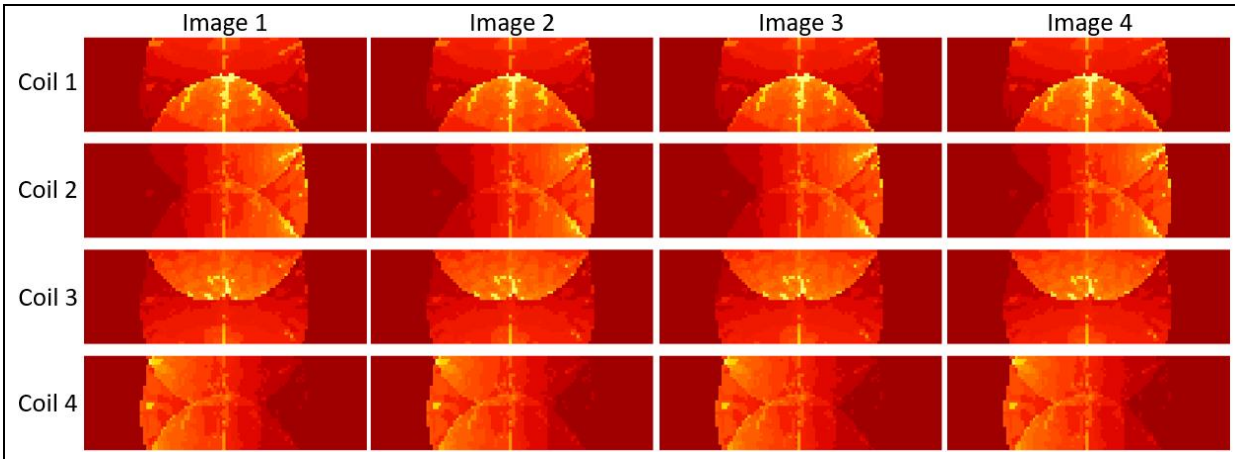

Figure 4.4: Simulated observed noisy magnitude coil images with incorporated coil covariance for a series of four images

$N(0, I_2 \otimes \Psi^{-1})$ noise that incorporates coil covariance to the noiseless coil images in Figure 2.8. The derived aliased noisy coil images are shown in Figure 4.4 and used to demonstrate the use of BSENSE for a series of images.

For the series of images, the MCMC Gibbs sampling technique will be utilized. The total number of iterations used was $L = 1000$ with a $burn = 200$. The observed aliased coil images in Figure 4.4 are coupled with the second model and its corresponding hyperparameters to estimate the final voxel values. The estimated voxel values v of the last $M = 800$ iterations in the Gibbs sampler for each image in the series were averaged together. The voxels are then unaliased and form the magnitude images shown in Figure 4.5.

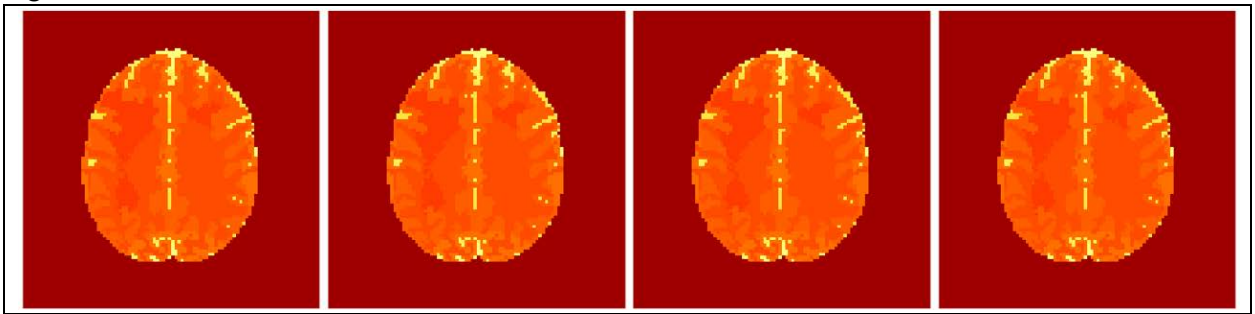

Figure 4.5: MCMC Gibbs sampling BSENSE series of $n_{IMG} = 4$ unaliased magnitude mean images that includes the induced coil and aliased voxel correlations.

This shows a successful reconstruction of a series of $n_{IM} = 4$ images where potentially induced coil covariance and voxel covariance is incorporated. Again, this process can be repeated with a larger number of images which can be used to create a time series of images. Figure 4.6 shows the magnitude variance images for the $n_{IM} = 4$ images in the series.

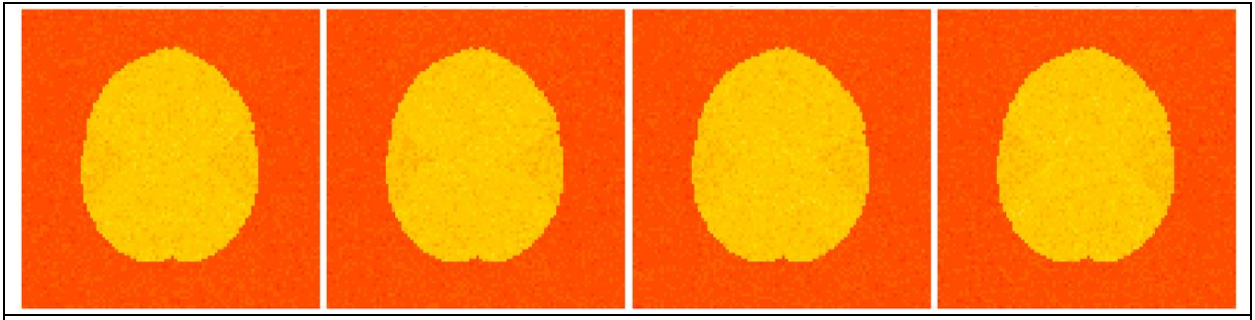

Figure 4.6: MCMC Gibbs sampling BSENSE series of $n_{IM} = 4$ unaliased magnitude variance images.

The magnitude variance images in Figure 4.6 show that the variance of the voxel is dependent upon the location of the voxel in the aliased images for all $n_{IM} = 4$ magnitude variance images. These results are similar to that of the single slice image in subsection 3.4.

5. Simulated Slice Images with Task Activation

5.1 Task Activation

The objective of fMRI is to have the patient perform a task, like tapping their fingers, and try to capture in which part of the brain increased neuronal activation occurs. The non-task reconstructed images essentially create a baseline value for each voxel giving us an intercept only simple linear regression $Y = \beta_0$, where Y is the estimated voxel value. By adding in task activation to a certain number of images in the series of images, we then have a simple linear regression $Y = \beta_0 + X\beta_1$ for our estimated voxel values where β_0 is the baseline voxel value from the non-task reconstructed images also known as the signal-to-noise ratio (SNR), β_1 is the estimated increase from β_0 which would be the contrast-to-noise ratio (CNR), and X is a vector of zeros and ones where the zeros correspond the images in the series without task activation and ones corresponding to the images with task activation. We can write this regression as $Y = X\beta$ where X is our $n_{IM} \times 2$ design matrix with ones in the first column and zeros and ones in the second column and β is a 2×1 vector containing $[\beta_0, \beta_1]'$.

With a typical increase in CNR being between zero and one, the task is not usually visual on the final reconstructed image. Instead, a hypothesis test is carried out with $\beta_1 = 0$ as the null hypothesis and $\beta_1 \neq 0$ as the alternative hypothesis. Eq 5.1 shows the simple two-tailed t-test with $\alpha = 0.05$ and sample size n equal to the number of images in the series.

$$t_{\beta_1} = \frac{\hat{\beta}_1}{SE\left(\hat{\beta}_1\right)} \qquad [5.1]$$

This will pinpoint the voxels that experience task activation. Figure 5.1 shows a small square of magnitude-only task equal to 0.5 being added to the true noiseless image.

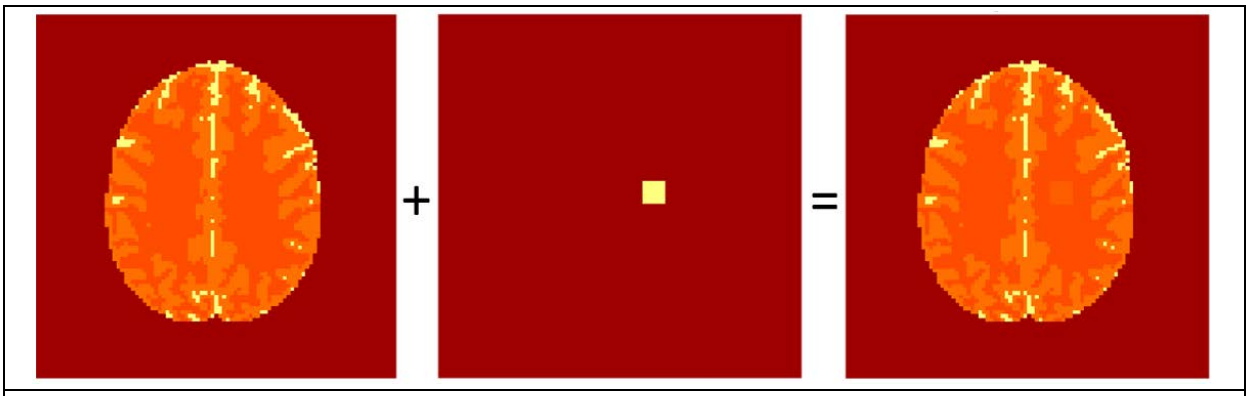

Figure 5.1: Adding magnitude-only task activation (middle) to the true noiseless image (left) to create the true task activation image (right)

5.2 Posterior Unaliased Image Results for Model One

Figure 5.2 displays the true magnitude, phase, real part, and imaginary part of the task activated image. A single task image was generated for $n_C = 4$ coils by adding $N(0, \sigma^2)$ noise to the

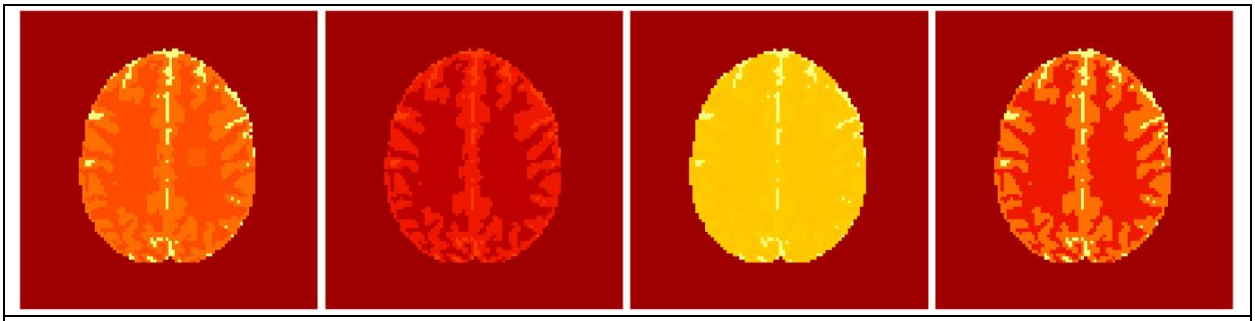

Figure 5.2: The true task activated images with magnitude (left), phase (left middle), real part (right middle), and imaginary part (right)

noiseless coil images in Figure 5.3. Since the amount of task added was 0.5 magnitude-only task, it is not visual in the simulated image. The derived aliased noisy coil images are used to demonstrate the use of BSENSE.

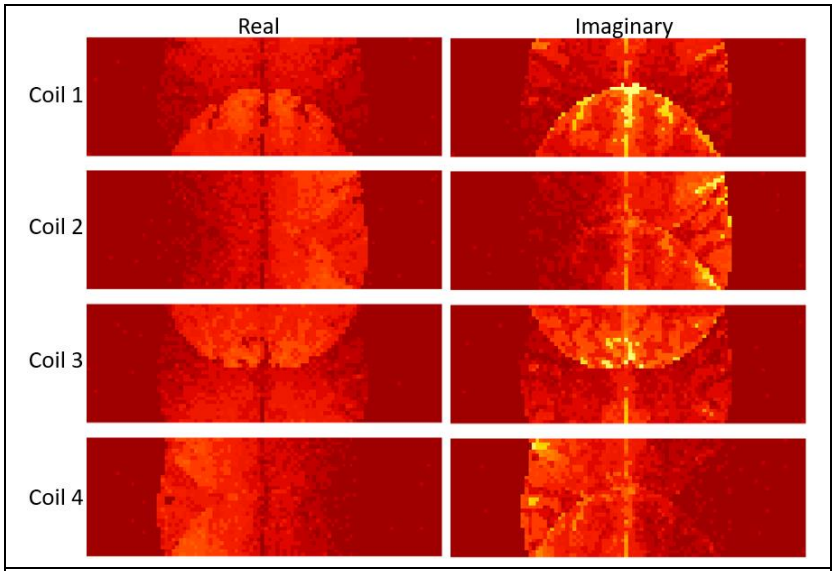

Figure 5.3: Simulated observed noisy coil images with task activation for one time point in an fMRI experiment.

The MCMC Gibbs sampling technique was utilized using a total of iterations $L = 10,000$ with a $burn = 2500$ to create the reconstructed final images. Note that the images in Figure 5.4 do not show the task as the CNR is small compared to the SNR and would need statistical analysis for any significantly greater voxel values.

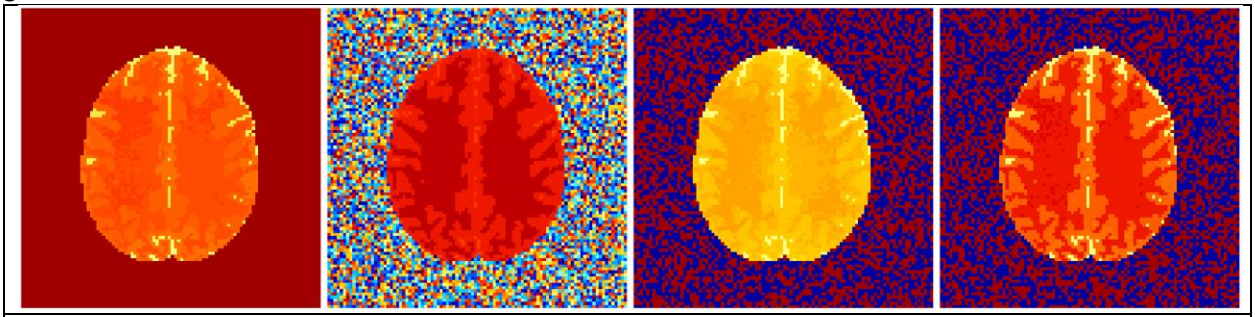

Figure 5.4: MCMC Gibbs sampling BSENSE unaliased mean images with no induced coil and aliased voxel correlations with magnitude (left), phase (left middle), real part (right middle), and imaginary part (right)

5.3 Posterior Unaliased Image Results for Model Two

This process was repeated using the second model by generating a single task image for $n_C = 4$ coils by adding $N(0, I_2 \otimes \Psi^{-1})$ noise to the noiseless coil images in Figure 5.5. The MCMC Gibbs sampling technique was utilized using a total of $L = 10,000$ iterations with a $burn = 2500$ to

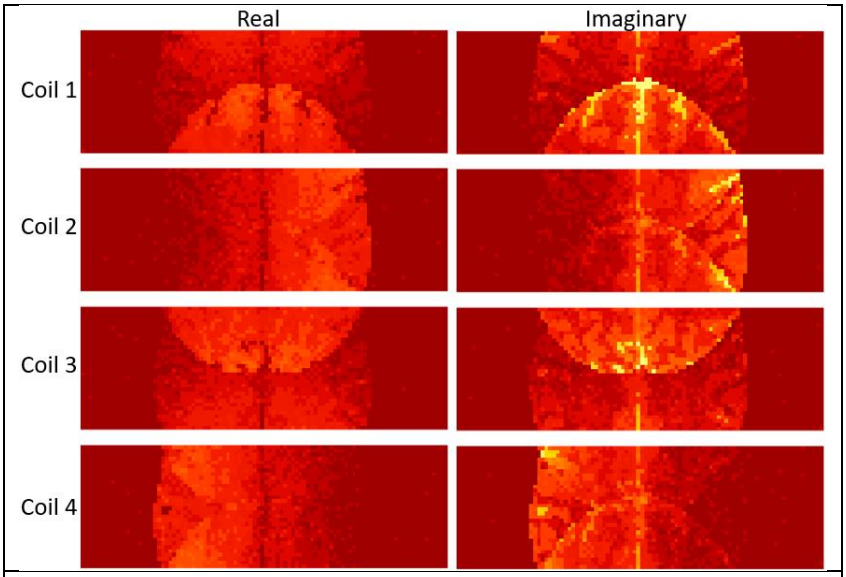

Figure 5.5: Simulated observed noisy coil images with task activation for one time point in an fMRI experiment.

create the reconstructed final images from the MCMC Gibbs sampler with 10,000 iterations and a burn of 2500 iterations are displayed in Figure 5.6. Again, note that the images in Figure 5.6 do not visibly show the task.

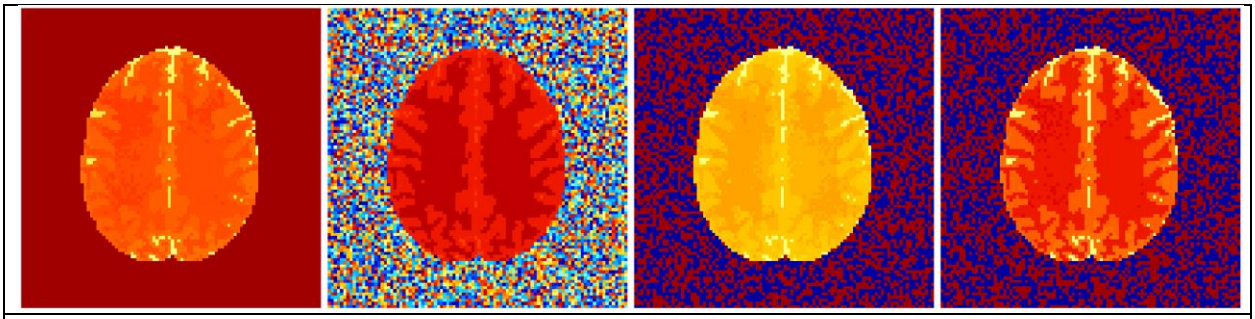

Figure 5.6: MCMC Gibbs sampling BSENSE unaliased mean images with no induced coil and aliased voxel correlations with magnitude (left), phase (left middle), real part (right middle), and imaginary part (right)

6. Discussion

6.1 Conclusion

Usage of parallel imaging techniques such as SENSE (Pruessmann et al., 1999) and GRAPPA (Griswold et al., 2002) have accomplished subsampling of the *k*-space reducing scan times for MR imaging. The inverse Fourier transformation of the subsampled *k*-space causes the images to be aliased so for SENSE image reconstruction, a least squares estimate is used to unalias the transformed image. This can be difficult to calculate if the design matrix is not full rank which, in general, is not so this paper introduces a Bayesian approach to estimate the unaliased voxel values. This method proposed two different models: one that does not account for potential coil covariance or aliased voxel covariance and one that incorporates both unobserved covariances.

Using calibrated images to assess for the hyperparameters, this approach successfully reconstructed a single slice simulated brain image using both models and a series of simulated slices without any aliasing artifacts. It also revealed no correlation from the unaliasing of the voxels which is an improved result from Sensitivity Encoding (Pruessmann et al., 1999).

6.2 Future Work

The next step for this research would be to run a MCMC Gibbs sampler series of images with some non-task images and the rest be images with simulated task activation. Then use the simple two-tailed t-test to detect the task activation in the voxels. After successful detection of task activation, BSENSE image reconstruction can also be used to examine different number of coils, whether it is 2, 4, 8, 16, or 32 coils, and altering the acceleration factors. These procedures can also be repeated for vertical aliasing as opposed to the horizontal aliased used in this research. Other potential work can involve aliasing three slices for a linearly summed image instead of three strips for each image. The goal of this research is to introduce and apply BSENSE image reconstruction to reduce the scan time of the fMRI process with comparisons to the traditional SENSE method along the way.

1. Bandettini P, Jesmanowicz A, Wong E, Hyde J. Processing strategies for time-course data sets in functional MRI of the human brain. Magn Reson Med 30:161–173, 1993.
2. Ogawa S, Lee TM, Nayak AS, Glynn P. Oxygenation-sensitive contrast in magnetic resonance image of rodent brain at high magnetic fields. Magn Reson Med 14(1):68–78, 1990.
3. Kumar A, Welti D, Ernst RR. NMR Fourier zeugmatography. J Magn Reson, 18(1):69–83, 1975.
4. Hyde JS, Jesmanowicz A, Froncisz W, Kneeland JB, Grist TM, Campagna NF. Parallel image acquisition from noninteracting local coils. J Magn Reson, 70:512–517, 1986.
5. Pruessmann KP, Weiger M, Scheidegger MB, Boesiger P. SENSE: Sensitivity Encoding for Fast MRI. Magn Reson Med, 42:952–962, 1999.
6. Griswold MA, Jamob PM, Heidemann RM, Nikkka M, Jellus V, Wang J, Kiefer B, Haase A. Generalized autocalibrating partially parallel acquisition (GRAPPA). Magn Reson Med, 47:1202–1210, 2002.
7. Rowe DB: Image Reconstruction in Functional MRI. In Handbook of Statistical Methods for Brain Signals and Images, Editors Ombao H, Lindquist M, Thompson W, Aston J. Chapman & Hall/CRC Press. p. 205-232, 2016.
8. Rowe DB, Logan BR. A complex way to compute fMRI activation. Neuroimage, 23:1078–1092, 2004.
9. Rowe DB. Modeling both the magnitude and phase of complex-valued fMRI data. Neuroimage, 25(4):1310–1324, 2005.
10. Lindley DV, Smith AFM, Bayes estimates for the linear model, Journal of the Royal Statistical Society B, 34 (1):1–18, 1972.
11. Geman S, Geman, D. Stochastic Relaxation, Gibbs Distributions, and the Bayesian Restoration of Images. IEEE Transactions on Pattern Analysis and Machine Intelligence. 6(6):721–741, 1984.
12. Rowe DB: Multivariate Bayesian Statistics: Models for Source Separation and Signal Unmixing. Chapman & Hall/CRC Press, Boca Raton, FL, 2003.
13. Bruce, Iain. *Determination of Correlations Induced by the SENSE and GRAPPA pMRI Models with an Application to MRI RF Coil Design*. 2014. Marquette University, PhD dissertation.